Beamforming Characterization of a Millimeter-wave

Reconfigurable Intelligent Surface

by

Brian Tjahjadi

A Thesis Presented in Partial Fulfillment
of the Requirements for the Degree
Master of Science

Approved July 2022 by the
Graduate Supervisory Committee:

Georgios Trichopoulos , Chair
James Aberle
Seyedmohammadreza Faghih Imani

ARIZONA STATE UNIVERSITY

August 2022

ABSTRACT

The reconfigurable intelligent surface (RIS) shown in this work is a programmable metasurface integrated with a dedicated microcontroller that redirects an impinging signal to the desired direction. Its characteristic allows the RIS to act as a mirror for microwave signals. Unlike a perfect electric conductor (PEC), the RIS has much more flexibility in redirecting signals. This work involves the measurement of a passive, fixed beam, 25x32 element mmWave RIS that operates at 28.5 GHz. Bistatic and monostatic measurement setups are both used to find the radar cross section (RCS) of the RIS. The process of creating the measurement setups and the final measurement results is discussed. The measurement setup is further characterized using the High-Frequency Structure Simulator (HFSS) software and the final measurement results are compared to analytical solutions computed using MATLAB.

The first prototype of the RIS has a loss of 8.4 dB when compared to a PEC and is physically curved. There is also a side lobe at the boresight of the RIS board that is only 8 dB less than the main beam in best-case scenario. This curvature causes issues with the monostatic measurement because it changes the phase that arrives at the RIS. The second prototype of the RIS has only 5.84 dB of loss compared to PEC. This measurement setup behaves mostly as expected when comparing the measurement results to the analytical solutions and given the limitations of the setup. A collimating lens was used as a part of the setup which reflects part of the incoming signal. The edge of the lens also causes diffraction. These factors contribute to multipath interference arriving at the receive antenna and increases measurement error. The lens also creates unequal amplitude illumination across the surface of the RIS which changes the RCS pattern. Using the lens

allows a more space-efficient setup while still obtaining relatively constant phase

illuminating across the RIS board.

ACKNOWLEDGEMENTS

I would like to thank Prof. Georgios Trichopoulos for the advising and mentoring throughout the duration of the thesis without which I would not be able to complete. I would also like to extend my thanks to my colleagues, Bharath Kashyap and Aditya Shekhawat for their support in lab and in discussions.

TABLE OF CONTENTS

LIST OF TABLES

LIST OF FIGURES

CHAPTER 1

INTRODUCTION TO RECONFIGURABLE INTELLIGENT SURFACES

Background

An RIS is a reflecting planar surface consisting of many sub-wavelength unit cells that can each apply a phase shift to impinging signals when it is reflected. Adjusting the phase shifts of each individual unit cell allows the RIS to redirect the impinging signal to the desired direction. An RIS can be classified as either an antenna-array structure or as a metasurface structure depending on its design [1]. The RIS characterized in this work is categorized as an antenna-array type. All RIS have some commonalities in their basic structure [2]. The topmost layer consists of sub-wavelength reflecting elements (microstrip patches). Below the top layer is a nearly solid copper plane to isolate the signal from the layers below. The bottom layers are responsible for controlling the phase shifts of each unit cell and is connected to a microcontroller. Controllers are needed to tune the RIS quickly to changes in the wireless environment. The phase shifts are usually tuned using either a varactor or positive-intrinsic-negative (PIN) diode. Varactor diodes provide continuous phase shifts but have performance issues with slow response times, inaccurate phase shifts, and have cutoff frequencies below mmWaves. Controlling them require analog controls which further complicates the RIS design. The parasitics on the varactor diode also prevent them from being used near mmWave and terahertz frequencies. In contrast, PIN diodes can only be turned on/off so they only provide discrete phase shifts but have faster response times, are simpler to integrate into an RIS, and can be used at mmWave frequencies.

1

In [3], a 60 GHz reconfigurable reflect array antenna was fabricated in 2009. To the author's knowledge, there was no other published work on reconfigurable reflect array antennas using single-bit quantized phase shifters at the time. The technique for 1-bit quantization used in that paper is very similar to the RIS that was measured in this work. Each reflecting element is connected to a PIN diode and the other side of the PIN diode is connected to a length of transmission line that is shorted to the ground. Although both reflect array antenna and RIS are designed to reflect incoming signals, there is a key difference between how they function. A reflect array antenna is fed by an antenna in the near field and excites the elements in the same way a typical array antenna would work. An RIS is expected to mostly work in the far-field and reflects that far-field signal instead of producing that signal locally. In a way, the RIS can be considered as a passive device. The RIS as a concept has only appeared recently due to advances in 5G and 6G. Although the technique for 1-bit phase quantization used in this RIS is not new, this RIS improves upon it by using phase randomization in the unit cells to remove the quantization lobe. [4]

The structure of the measured RIS is shown in figure 1.1. Looking at the bottom layer, this is done using an PIN diode that can be switched on/off using a control board. A 1-bit quantization scheme is used because only 2 states are available (on/off) with the PIN diode. The PIN diode is approximated as an ideal switch where it is an open in the 'off' state and a short in the 'on' state. When the PIN diode is 'off' the signal sees an open and is reflected back to the antenna; however, if the PIN diode is 'on' then the signal will see a short and travel down the line until it encounters a via short to ground where it will also be reflected back to the antenna. Ideally, the phase difference in the

reflection of these two states should be 180° across the frequency range which gives rise to the 1-bit quantization scheme [4].
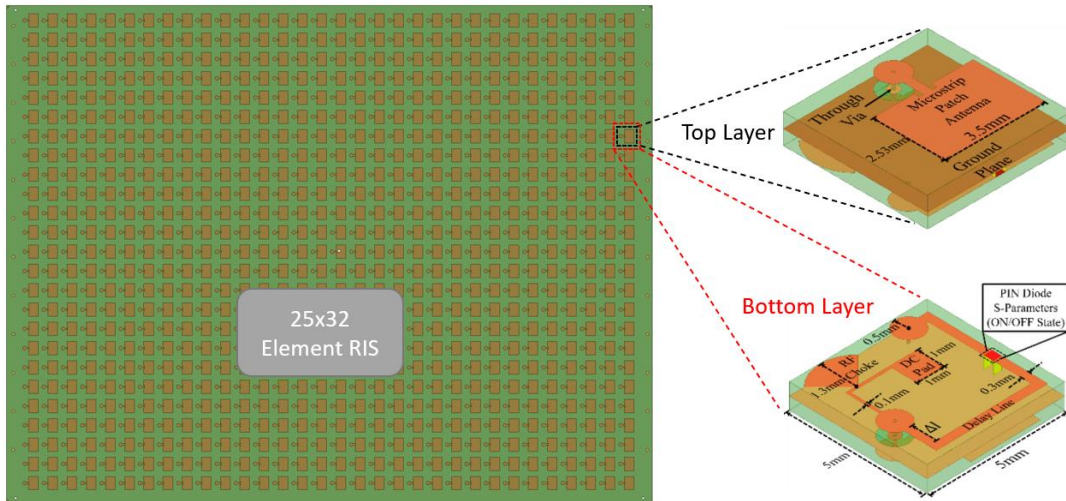
Figure 1.1: Geometry of RIS Being Measured. Top and Bottom Layer of Each Unit Cell is Shown

This measurement concerns a passive version of the RIS that is configured to redirect an incoming signal from the boresight of the RIS to θ=30°, Φ=0° (and vice versa). A control board is not necessary to operate the RIS and the PIN diodes are replaced with a physical short and open. This version of the RIS has 25 x 32 elements. The nominal frequency of operation of the measured RIS is 28.5 GHz which is in the mmWave frequency.

Application

        One of the original goals of 5G was to incorporate mmWave communication for high data rate and low latency communication. However, mmWave communication was not widely adopted in 5G due to its many challenges and is planned for 6G instead. Signals at mmWave frequencies suffer from high path loss and high attenuation from blockages which only allows limited coverage. High path loss can be offset with electrically large high gain arrays, but the problem of blockage persists. RIS aims to solve the blockage problem at mmWave frequencies while minimizing hardware costs and power consumption. The low profile of the RIS also allows it to be placed on ceilings, walls, signs, streetlamps, buildings, and many other places.

        One of the standard methods of solving blockage problems is to use an active relay which regenerates signal and retransmits them. This requires a power amplifier and other active components which increases hardware costs and power consumption. There is a tradeoff between data rate and cost depending on whether a half-duplex or full-duplex relay is used. A successful implementation of the RIS can have the advantages of both types of relays. In contrast to the relays, the RIS acts as a mostly passive device that redirects the signal, only little power is needed to bias the PIN diodes and power the control board.

        A case study in [1] evaluates the achievable sum rate for a hypothetical scenario with different RIS configurations. The case study performed a simulation that involves 2 base stations at opposite ends of the test range and a group of users in between them. Some blockage is assumed between the direct line of sight path from the base stations to

the users and a value of path loss exponent is assigned for this path. Then an RIS is placed in a way that avoids this blockage and the path from the base station -> RIS and from RIS -> user has a lower path loss exponent while having a longer total distance. The simulation tests 3 different cases; no RIS, RIS using random phase shifts, and optimal phase shifts for the RIS. Results in that paper show that even the RIS using random phase shifts can achieve slightly higher sum rates than not using an RIS at all and an optimized RIS can achieve much greater sum rates than the other 2 cases.

The properties of the RIS makes it useful for several applications and scenarios. Applications such as virtual reality (VR) benefit from offloading the computation to a computing node rather than performing all the calculations on the VR device itself because of its limited power and hardware. If the VR device is at the edge of the network, it will suffer from low data offloading leading to higher latency. The RIS can improve data rate for offloading computation by avoiding blockages and improve latency for VR applications. The RIS also helps in scenarios where there are multiple base stations using the same frequency spectrum each servicing different cells. There will be considerable interference for users at the cell edge who are almost equidistant from multiple base stations which will result in low signal-to-interference-plus-noise ratio (SINR). Deploying RISs at the cell edges can enhance the received power for those users and reduce interference simultaneously. At the same time, the RIS also has the capability to increase interference to users. This should be avoided in the scenarios mentioned above but can be useful to prevent eavesdroppers from intercepting communication and increase received power to legitimate users for secure applications. In [5], an RIS based posture-sensing recognition system was developed. Radio frequency (RF) sensing for posture

5

recognition needs multiple transceivers to accurately obtain 3D information. The

transceivers cause multi-path fading which is exacerbated by having multiples of them.

Using an RIS can help manage these unwanted paths and create beneficial paths instead.

This will end up increasing the accuracy of the posture recognition. These are just some

of the interesting applications of RIS on the internet of things (IoT) and future 6G

technology but is by no means an exhaustive list.

State-of-the-Art Research

A 2-bit phase quantized RIS was developed recently in [6] at 2.3 GHz. Most other RIS uses 1-bit phase quantization because of complexity and space constraints for such small area of unit cell. The 2-bit phase quantization was achieved using a slot-loaded plane placed between the patch antenna and the ground plane. A total of 5 PIN diodes were connected to the slots but only 2 control signals were needed to operate them. The 2 controls signals allow for 4 different configurations for biasing the PIN diodes. Depending on the configuration, the RF current travels along different paths in the slots which gives rise to the different phase shifts.

A unique RIS was developed in [7] where it can do both amplitude and phase modulation. The RIS uses varactor diodes for analog tuning, but this RIS only operates at a low frequency of 4.25 GHz. Although the authors consider their work as an RIS, it functions more similarly to a reflect array antenna rather than a typical RIS. Usually, an RIS merely redirects an already modulated signal from some transmitter. The RIS used in their work acts as a transmitter that is illuminated by a nearby antenna just like a reflect array antenna. This type of RIS would have very different applications compared to a typical RIS. The unique part about this RIS is that it is fed an unmodulated carrier signal from a feed antenna in the far-field. The RIS then modulates the phase and amplitude of the signal based on information from the digital baseband module that is attached directly to the RIS. In essence, the RIS allows the transmitter system to skip the conventional RF chain and do the modulating on the RIS itself. Only a narrowband power amplifier is needed at the feed antenna.

7

Many RIS (including the one characterized in this work) often have patches connected to the ground through a PIN diode which is used to control the reflection phase. In [8], an RIS was developed using a parasitic resonator which is capacitively coupled to a patch reflector. The parasitic resonator is loaded with a PIN diode that controls the reflection phase. This method provides a larger bandwidth and reduces power dissipation. It shares the same frequency of operation (28.5 GHz) and 1-bit phase quantization as the RIS characterized in this work. That work also demonstrates how its RIS can remove the quantization lobe by illuminating the RIS with a spherical wave instead of a plane wave.

Most of state-of-the-art research does not focus on just the hardware of the RIS itself. The second example in this section not only deals with the physical hardware of the RIS but also the overall architecture of the RIS-based transmitter system and modulation techniques. Many of the research deals with signal processing, algorithms with learning capabilities, case studies relating to data rate or received power, optimum deployment of RIS and additional sensor capabilities. [9]

Radar Cross Section Characterization

At mmWave frequencies, the unit cell of the RIS becomes very small and a high gain RIS can be fabricated with many elements. The RIS measured in this work has 800 elements in total with 5 mm element spacing which is just under half a wavelength. However, this presents a challenge for measurement in the far-field because the RIS is electrically very large. A spacious test range is needed to perform the measurement at far-field. Having a compact antenna test range would be desirable for such a measurement.

One of the cited works [6] uses a compact range reflector in an anechoic chamber to measure one of their RIS. That work presents an RIS that operates at 2.3 GHz and claims to have a 28.5 GHz version but only the 2.3 GHz version of the RIS was measured in the anechoic chamber. This is likely because the antenna test range was unsuitable for mmWave frequency. The anechoic chamber at ASU that contains a reflector also does not operate up to 28.5 GHz. A single collimating lens was used in place of a reflector in the measurement setup located inside the lab.

According to [10], the collimating effects of a reflector in a compact test range reduces the importance of having a high-quality absorber at the chamber's walls, floors, and ceilings. This can be extended to collimating lenses as well. However, a quality absorber at the end wall of the chamber is still needed. The setup in the lab uses absorbers behind the measured RIS but not many at other places.

In [3] and [11], the performance of the reflect array antennas were calibrated or normalized to that of a conductor plate. The performance of the measured RIS in this work was also compared to that of a PEC since they all act as mirrors for RF signals. The

measurement setup proposed in [11] is also similar to the one used in lab except the transmit antenna is much closer to the device under test (DUT) since they were trying to feed the reflect array from the near-field. Another minor difference is that the DUT rotates with the transmit antenna while the RIS measured in lab is fixed in place and always facing the receive antenna.

The paper in [12] shows a couple of interesting techniques for RCS measurements. RCS is a measure of how much reflected energy is detected when compared to an isotropic reflector. The RIS is compared to a PEC of similar size instead of an isotropic reflector so the value of the RCS is not directly important. Nevertheless, some of the techniques shown in that paper can be useful for this type of measurement. The formula for the uncertainty of an RCS measurement is shown below where ϵ is the ratio between the target reflected power and the reflected power from the environment in. Both $\Delta\sigma$ and ϵ are in dB.

$$\Delta\sigma = -20\log\left(1 - 10^{\frac{-\epsilon}{20}}\right) \tag{1}$$

This formula shows that if the reflected power from the target is at least 20 dB higher than the reflected power from the environment, the uncertainty in the measurement will be within 1 dB. Another way to eliminate uncertainties in measurement other than having a lower reflection environment is to use signal processing techniques such as time gating and background subtraction.

CHAPTER 2

RCS PATTERN MEASUREMENT USING BISTATIC SETUP

Description of Bistatic Setup

This section concerns the measurement of the RCS pattern using a bistatic setup. The Rx antenna stays at a fixed location while the Tx antenna is mounted on the optical rail and rotates around the RIS. The received signal power level is recorded at regular degree intervals and the resulting pattern is obtained. The same measurement is also performed on a copper plate (approximated as a PEC) in place of the RIS. Measurement results with the PEC acts as a reference for the power levels obtained with the RIS because it acts like an ideal mirror. The PEC is the same size as the RIS to keep the aperture area the same. Unlike the RIS which is facing the Rx antenna (zero degrees), the PEC is placed facing 30° away from the Rx antenna to keep the aperture area the same when measuring their max received power.
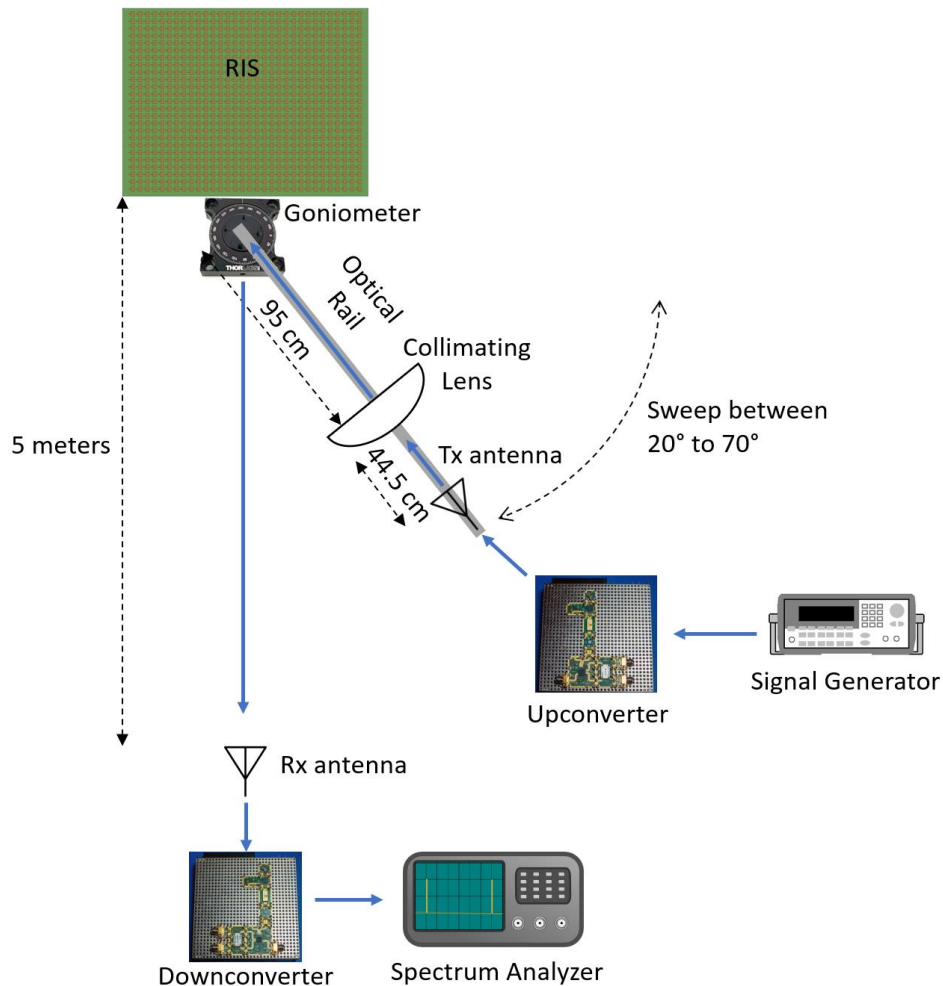
Figure 2.1: Diagram for Bistatic Measurement Setup

Both the signal generator and spectrum analyzer only work up to 3 GHz so an

upconverter and downconverter are needed for measurement at 28.5 GHz (the nominal

frequency of the RIS). The models of the upconverter and downconverter are the

ADMV1013 and ADMV1014 respectively from X-Microwave. These are controlled

using a raspberry-pi based touchscreen controller also provided by X-Microwave.

To use the upconverter/downconverter, add the part 'ADF5356' on the controller.

This is the VCO that's used in both the upconverter and downconverter. Set the

'Reference freq' to 100 MHz. The 'desired RF A Freq' can be changed to get the LO

frequency to whatever is needed. There is an 8x frequency multiplier in the RF chain.

The settings used for operation at 28.5 GHz RF frequency are 3250 MHz for the

upconverter and 3875 MHz for the downconverter which corresponds to an LO frequency

of 26 GHz and 31 GHz respectively. This is assuming the desired IF is 2.5 GHz. It was

found empirically that these settings produced the highest power level at the receiver

which will help with the dynamic range of the test setup to detect sidelobes. The

upconverter and downconverter filters one of the sidebands (lower or upper) which

explains this phenomenon. The same steps are used to setup the upconverter and

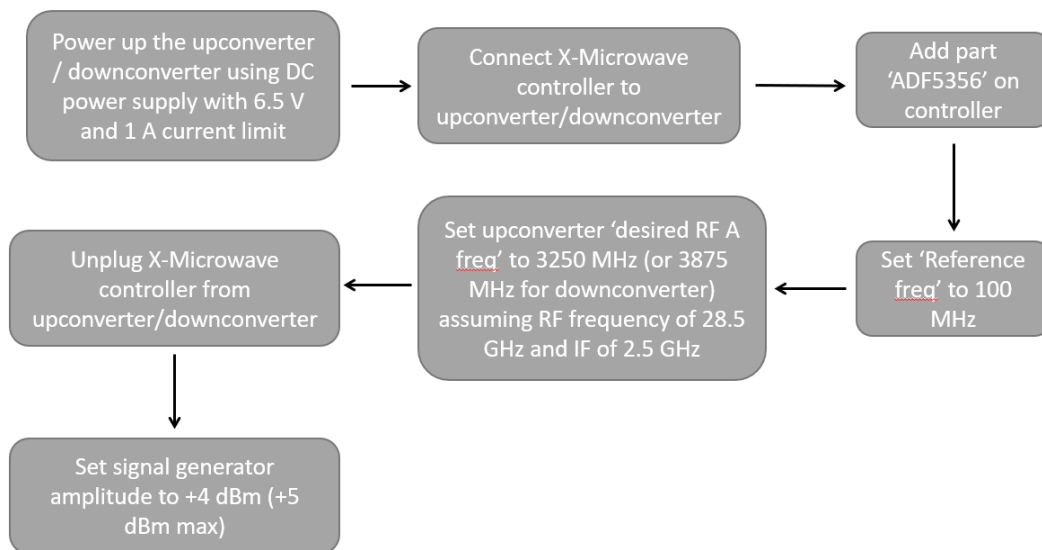downconverter except for the value used in 'desired RF A Freq'.

```
┌─────────────────────┐     ┌─────────────────────┐     ┌─────────────────┐
│ Power up the        │     │                     │     │ Add part        │
│ upconverter /       │     │ Connect X-Microwave │     │ 'ADF5356' on    │
│ downconverter using │ ──▶ │ controller to       │ ──▶ │ controller      │
│ DC power supply     │     │ upconverter/        │     │                 │
│ with 6.5 V and 1 A  │     │ downconverter       │     │                 │
│ current limit       │     │                     │     │                 │
└─────────────────────┘     └─────────────────────┘     └─────────────────┘
                                                                  │
                                                                  ▼
┌─────────────────────┐     ┌─────────────────────┐     ┌─────────────────┐
│                     │     │ Set upconverter     │     │                 │
│ Unplug X-Microwave  │     │ 'desired RF A freq' │     │ Set 'Reference  │
│ controller from     │ ◀── │ to 3250 MHz (or     │ ◀── │ freq' to 100    │
│ upconverter/        │     │ 3875 MHz for        │     │ MHz             │
│ downconverter       │     │ downconverter)      │     │                 │
│                     │     │ assuming RF         │     │                 │
│                     │     │ frequency of 28.5   │     │                 │
│                     │     │ GHz and IF of 2.5   │     │                 │
│                     │     │ GHz                 │     │                 │
└─────────────────────┘     └─────────────────────┘     └─────────────────┘
         │
         ▼
┌─────────────────────┐
│ Set signal          │
│ generator amplitude │
│ to +4 dBm (+5       │
│ dBm max)            │
└─────────────────────┘
```

Figure 2.2: Flowchart for Using the X-Microwave Controller and Signal Generator

Iteration Process to Achieve Final Setup

The physical setup for the bistatic measurement went through many iterations due to reliability issues. A bad alignment of the measured object (RIS or PEC) significantly affects the power received at the antenna. Alignment of the Tx antenna is also important and to a lesser extent the Rx antenna. The antenna used in this measurement is the WiseWave ARH-28 15-02 which is a 15 dB rectangular horn antenna with a frequency range of 26.5 GHz to 40 GHz. It is a relatively low gain horn antenna which is why alignment of the antennas is less sensitive compared to the RCS object. However, the transmitting antenna is much closer to the measured object and a PTFE lens is placed nearby to collimate the beam. This explains why the alignment of the Rx antenna was less sensitive compared to the Tx antenna.
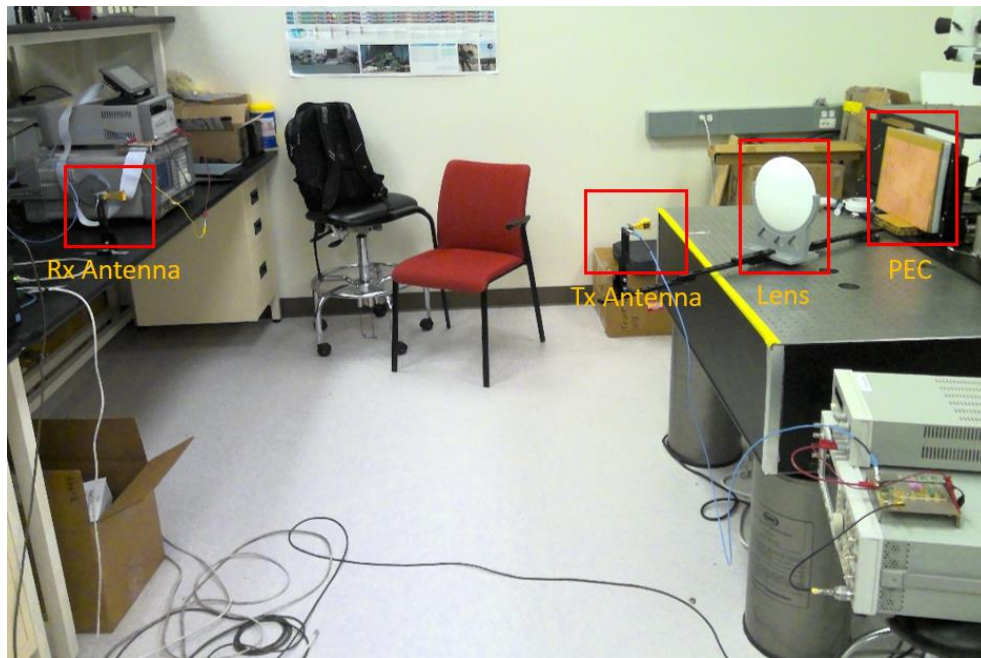
Figure 2.3: Preliminary Setup for Bistatic Measurement

This setup is just to test if a signal can be detected at the spectrum analyzer (on the left). The fixture for the PEC is made of cardboard and is not yet carefully positioned. The PEC here is not cut to the same size as the RIS and the Rx antenna on the left is not far away enough to be in the far-field. Sometimes, the X-microwave controller and upconverter / downconverter were not working at all or working incorrectly.

There was a lot of multipath interference that were being picked up by the Rx antenna. This was apparent after testing with an absorber and standing near the Rx antenna at various angles. The received power level would reduce even though the absorber was not blocking the specular direction from the PEC.
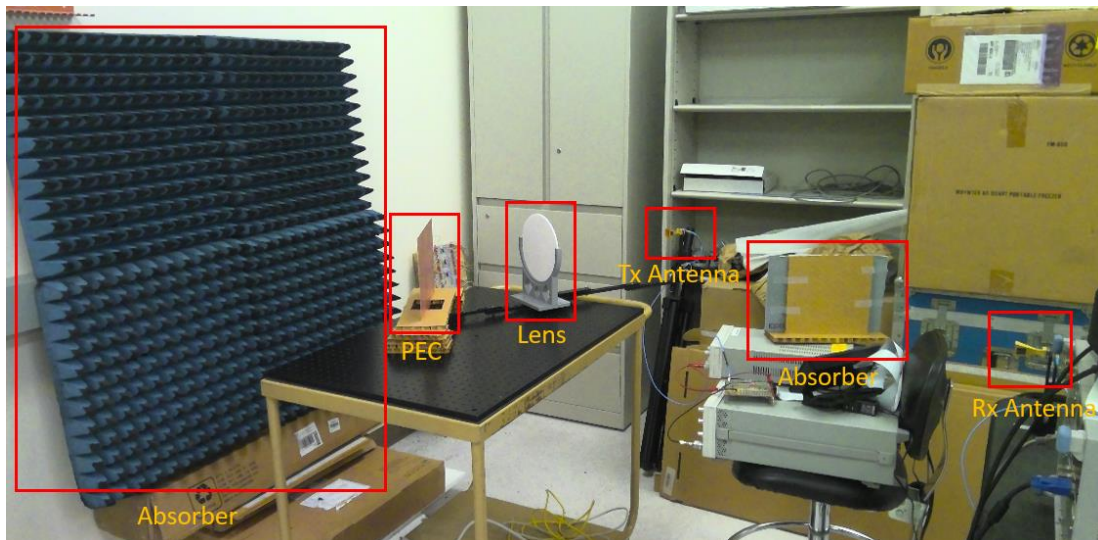
Figure 2.4: Bistatic Measurement Setup to Reduce Interference

The setup in figure 2.4 tries to mitigate some of the problems in the preliminary setup. It was moved to a different location so there would be space to put absorbers behind. Another small piece of absorber was placed between the Tx and Rx antenna which helped reduce the received power level a little. At the time of this setup, it was

thought that the additional received power at the receiver was caused by the sidelobes of the Tx antenna coupling to the Rx antenna. It was later found to be caused by a portion of the signal reflecting off the lens, although most of it still passes through. The fixture for the copper plate was still made of cardboard but it was now centered on top of the goniometer. The received power level at the spectrum analyzer varied a lot between measurements because the cardboard fixture is flimsy and makes the PEC tilt differently each time it was placed on the fixture. Slight differences in the tilt could change the received power level by more than 20 dB which shows how sensitive the alignment is.
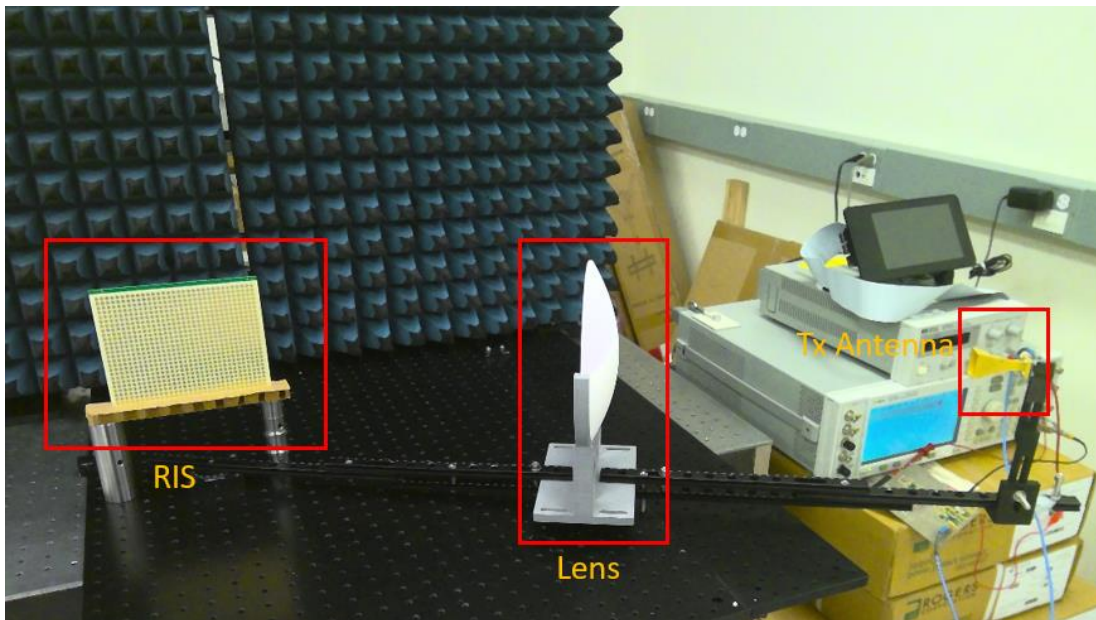
Figure 2.5: Attempted Far-Field Setup for Bistatic Measurement. Shows RIS and Tx Antenna
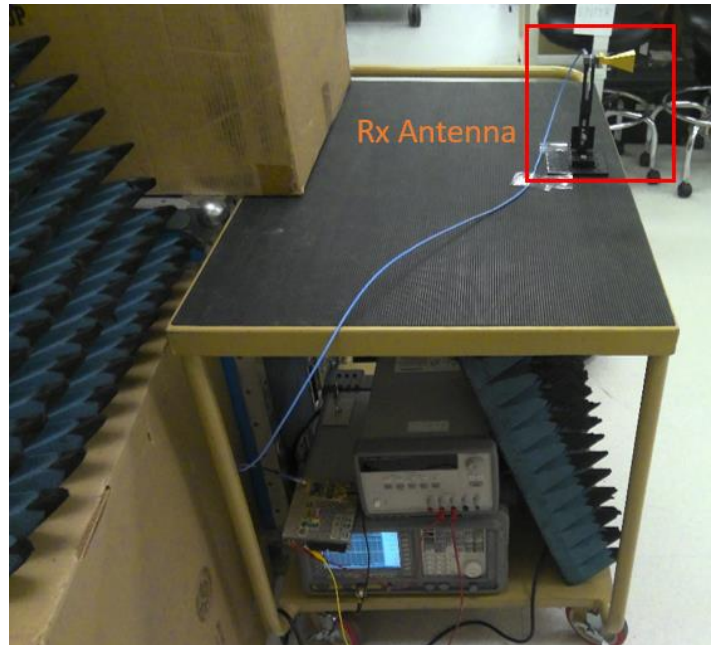
Figure 2.6: Rx Antenna Setup 5 Meters Away from the RIS

The measurement setup was moved again so there is enough space for far-field

radiation to the Rx antenna which is about 5 meters away from the RIS. The calculation

for far- field is shown using D = 0.168 meters (RIS is 13.9 cm x 16.8 cm) in equation 1.

There was not enough space in the lab for more than 5 meters. The Tx antenna can be

placed much closer to the RIS because the lens turns a spherical wave into a plane wave

when the spherical wave originates from the focal point. Some of the components such as

the upconverter and X-microwave controller were faulty and swapped for a spare unit

that was available. They were sometimes not turning on at all or the frequency that was

outputted was incorrect. It is also a good idea to unplug the X-microwave controller from

the upconverter/downconverter after loading the settings onto them. The X-microwave

controller sometimes sends unintended data to the upconverter/downconverter when left

attached for too long which causes the frequency at the spectrum analyzer to suddenly

change in the middle of measurement. Absorbers were placed around the setup as a

precaution.

$$Far-field\ distance: \frac{2D^2}{\lambda} = 5.36\ m\ \approx 5\ m \qquad (2)$$

However, there were still a lot of problems with this setup. Multiple optical rails

were attached together to give the needed length but makes them easy to bend. The

weight of the lens makes them flex downwards and causes the Tx antenna to tilt up a

little bit. When the optical rails are straightened, the received power level at the spectrum

analyzer increases. The distance between the RIS and the lens is 44.5 cm which is the

focal distance of the lens to obtain minimum beam radius (waist of the beam). However,

at this distance, the diameter of the lens was wide enough to impact the reflected signal

when sweeping the Tx antenna near boresight. When the distance between the RIS and

the lens was increased to 95 cm this behavior no longer occurred. Table 1 shows how the

received power levels were affected as the Tx approaches 0 degrees.

Table 2.1: Received Power Levels When PEC is 44.5 cm from Lens

Angle of PEC from Rx Antenna (°)	Received Power Level (dBm)
20	-17.52
25	-14.7
30	-13.41
35	-14.2

The aperture area increases when the PEC is facing smaller angles, directivity

should increase and so the received power level was expected to increase as well. On the

contrary, the received power level suddenly dropped to -17.52 dBm at 20° and dropped slightly at 25° when compared to the received power level at 30°. It makes sense for the power level to drop at 35° when compared to 30° since aperture area is smaller. The PEC can be compared to a planar array where the directivity decreases as θ_o increases (θ_o is angle from boresight). The $cos\theta_o$ term is the decrease in directivity caused by a decrease in the projected area of an array. Another way to look at it is using equation 3 where the directivity decreases when the aperture area also decreases. Intuitively, the effective aperture area looks smaller when looking at it from an angle.

$$Directivity\ of\ planar\ array: D_o = \pi\ cos\theta_o D_x D_y \qquad (3)$$

$$Directivity\ of\ aperture\ antenna: D_o = \frac{4\pi}{\lambda^2} A_p \qquad (4)$$

It should be mentioned that when the PEC is facing say 20°, the Tx antenna should then be at 40°. The Tx antenna should be placed at an angle that is double compared to the angle the PEC is facing. The PEC acts like a mirror and Snell's law states that the incident angle is equal to the reflected angle. This means the reflected signal will be travel towards 0° which is facing the Rx antenna, giving the maximum receiver power at the spectrum analyzer.
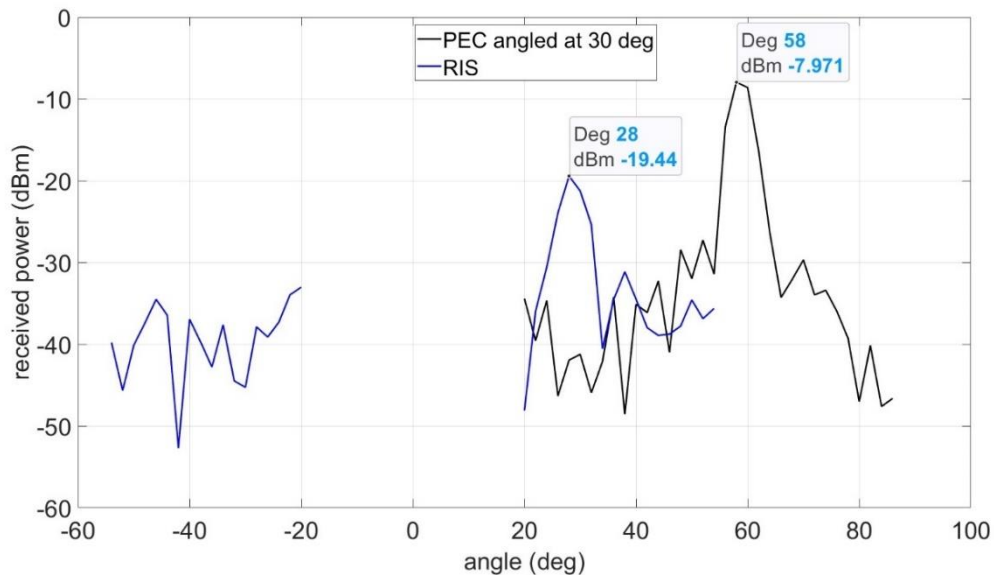
Figure 2.7: Measured Received Power for RIS and PEC Every 2° (Cardboard Fixture Setup)

These measurements show that there is a large difference between the reflected power by the PEC and the RIS, about 11.47 dB difference between the max of the RIS and the PEC. It was observed many times that the imperfections in the alignment cause a large drop in received power level even if they seem small to the naked eye. Improvements needed to be made to the fixture for the RIS to make it reliable and easy to adjust.
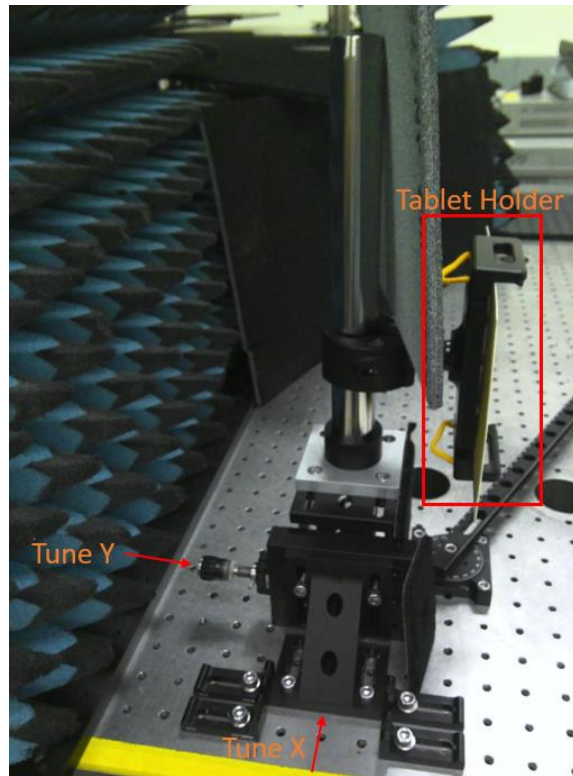
Figure 2.8: Adjustable Fixture Using Optical Bench Equipment (Preliminary)

A new fixture was built using optical bench parts and a tablet holder. Adjustments can be made more accurately with more degrees of freedom compared to the previous fixture. Displacement in the X and Y axis can be tuned so that the RIS can be centered on top of the goniometer and the tablet holder can swivel around freely. The received power level increased compared to previous setups which indicates the alignment had improved.
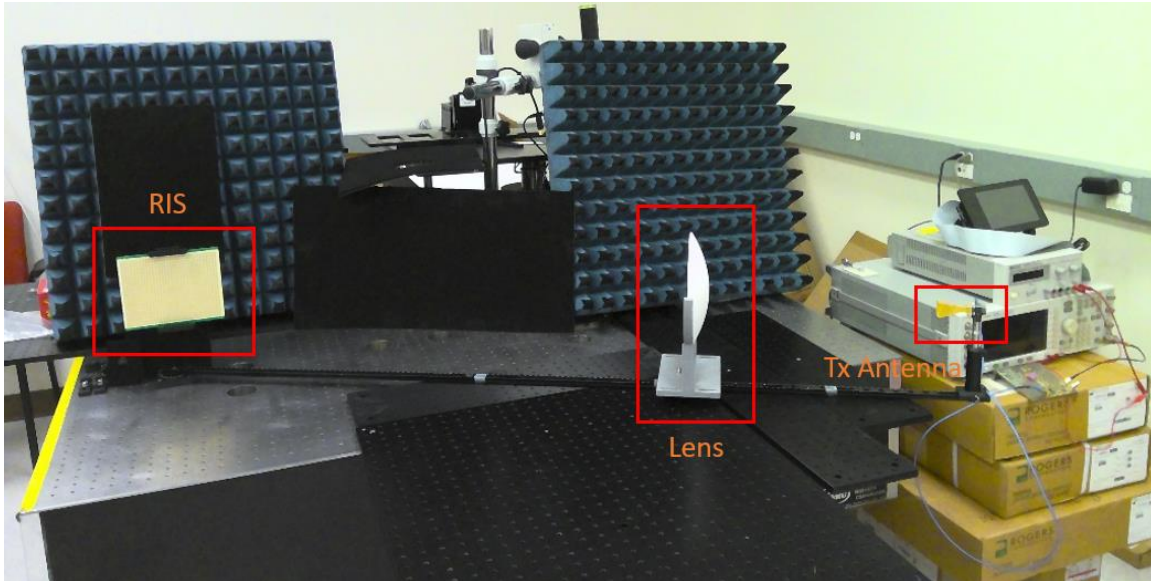
Figure 2.9: Distance Between Lens and RIS Increased from 44.5 cm to 95 cm

Increasing the distance between the lens and RIS allows the setup to rotate closer to boresight (0 degrees) without adversely affecting the reflected signal. Optical breadboards were attached to the optical bench to extend the platform which provides physical support to the setup. The lens is heavy and so there needs to be something underneath to support it. There is a wooden beam supporting the optical breadboard otherwise the optical breadboard will sag. The platform underneath the optical rail needs to be flat otherwise the Tx antenna will not be level.
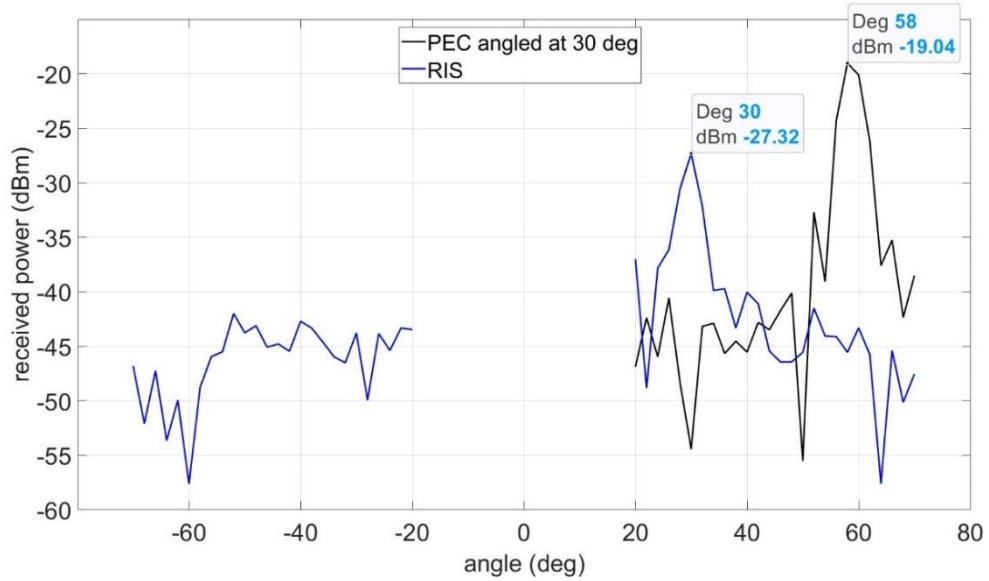
Figure 2.10: Measured Received Power for RIS and PEC Every 2° (Preliminary Adjustable Fixture)

The difference between the max value of the RIS and PEC is now at 8.28 dB compared to 11.47 dB previously. Inconsistent tilting when measuring the RIS and PEC was no longer an issue. It was observed that alignment of the pitch angle is very sensitive. Adjusting the tablet holder for pitch angle alignment was difficult, time-consuming, and generally unreliable. Changes needed to be made to the fixture for continuing additional measurements.
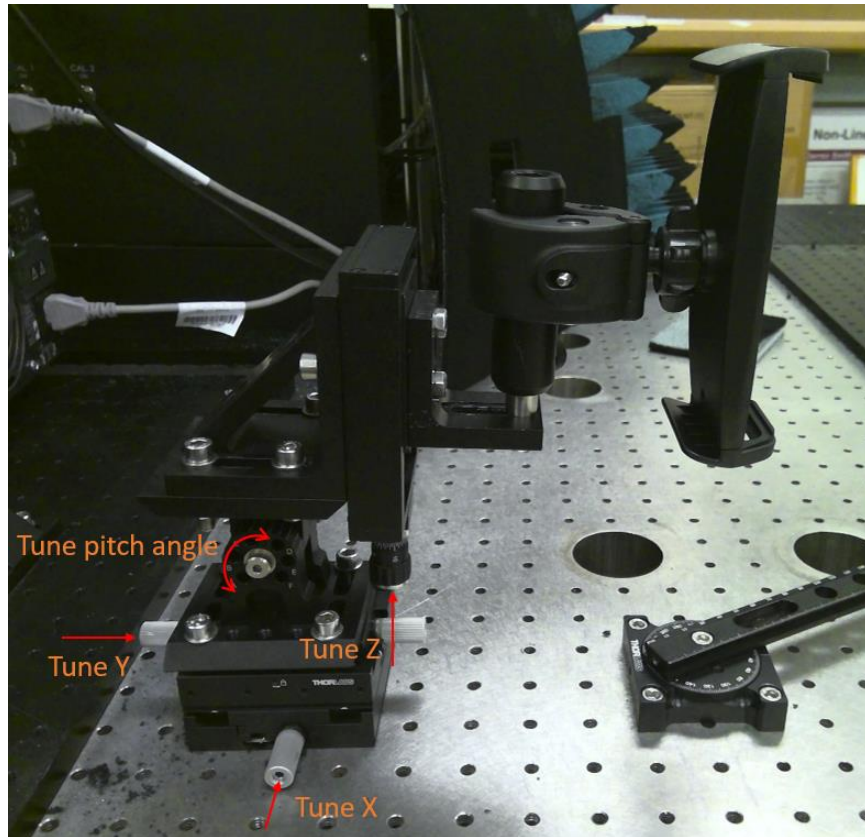
Figure 2.11: Updated Adjustable Fixture

With this new adjustable fixture, displacement in the XYZ axis and pitch angle can all be finely tuned. Yaw and roll angle can also be tuned using the tablet holder but not as finely. The tablet holder has been replaced with a different one to accommodate the control board's larger size. In this case, the control board cannot change the phases of the unit cells in the RIS since this is the passive version of the RIS. The RIS board is curved to one side because of an uneven amount of metal on one side of the PCB compared to the other side. Mounting the RIS to the control board straightens the RIS. It would also be useful to find unexpected side effects of the control board to the RCS pattern of the RIS.
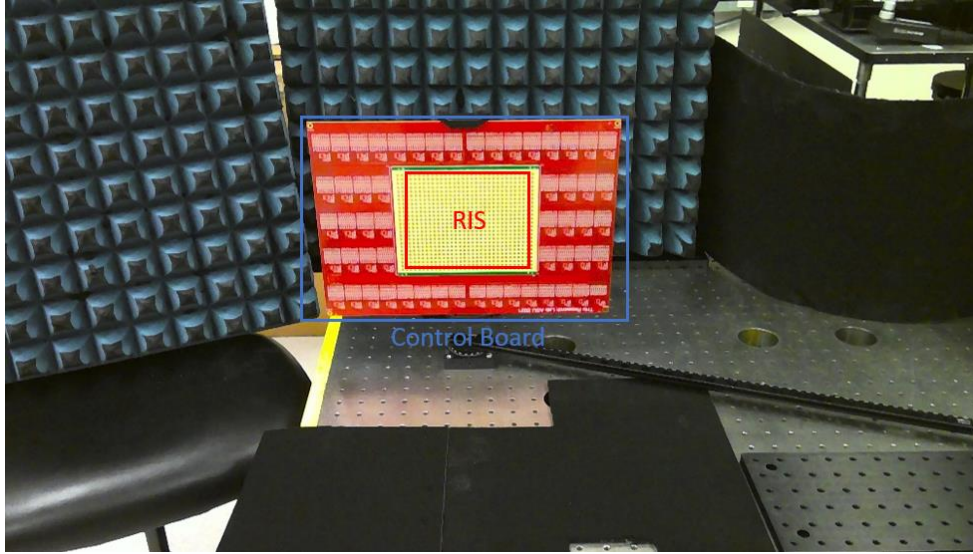
Figure 2.12: RIS Mounted on the Control Board
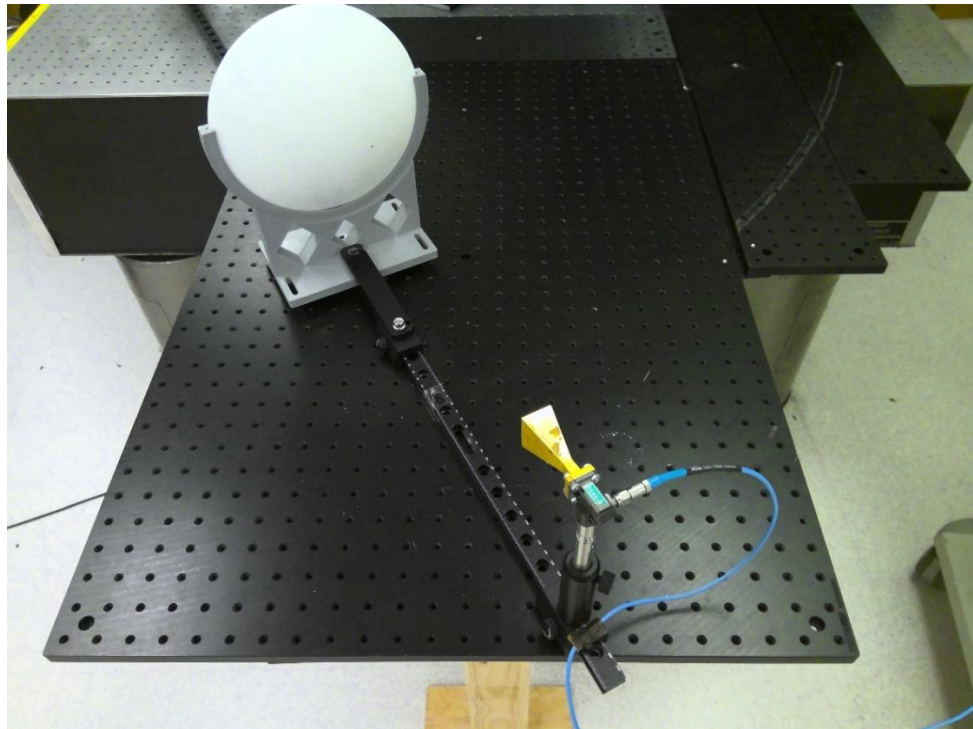
Figure 2.13: Lens and Tx Antenna Mounted on Optical Rail
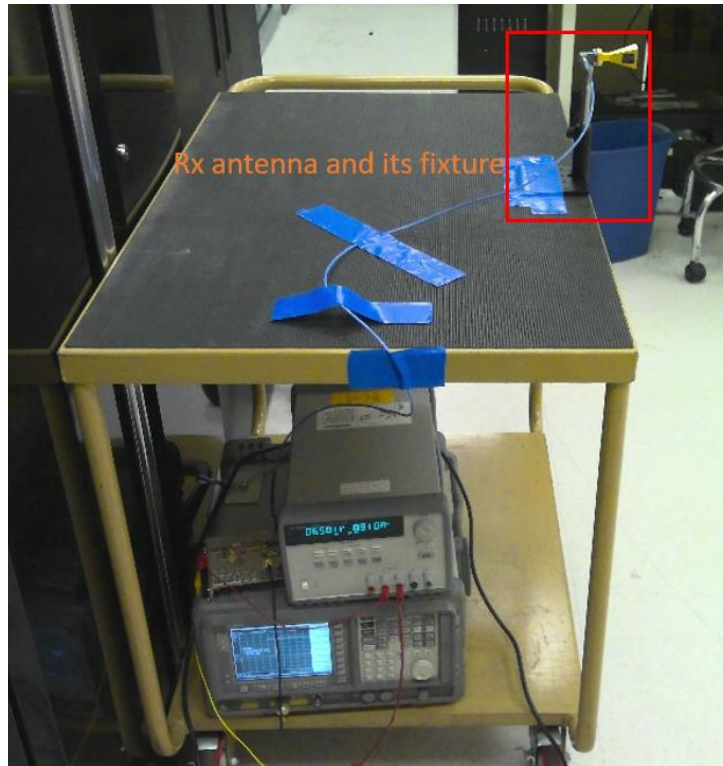
Figure 2.14: Rx Antenna on New Fixture

The lens and Tx antenna were also mounted on the optical rails in a way where they can be adjusted along the rail. Adjusting the height and swivel of the Tx antenna is also possible. 5 meters away from the RIS is the Rx antenna with the downconverter and spectrum analyzer underneath the cart. The height of the Rx antenna can be adjusted.

Measurement Results Using Final Setup
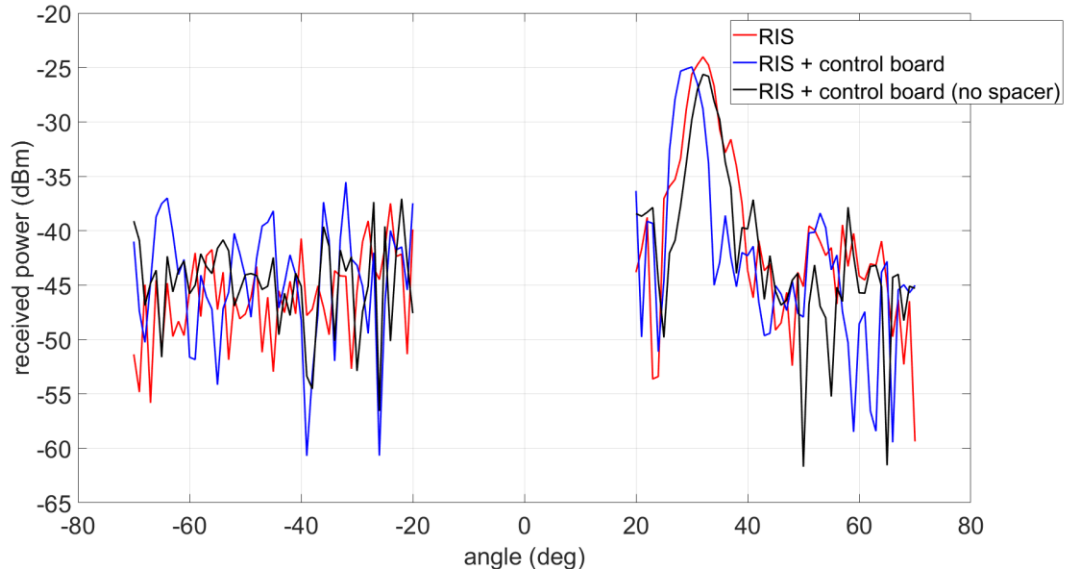
Figure 2.15: Bistatic Measurement Result at Nominal Frequency of 28.5 GHz for Various Board Configuration (Measured Every 1°)
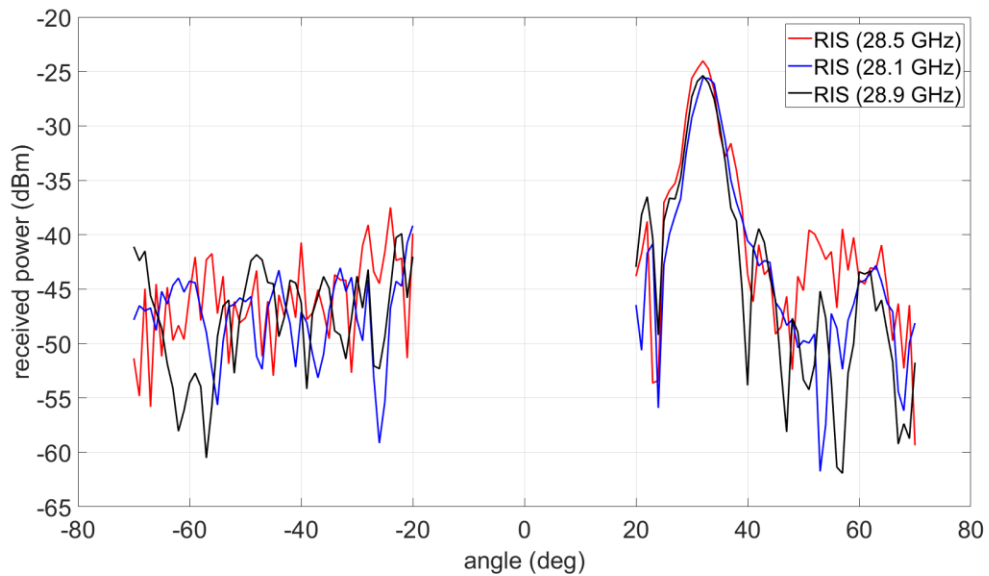
Figure 2.16: Bistatic Measurement Result for Standalone RIS at Different Frequencies (Measured Every 1°)
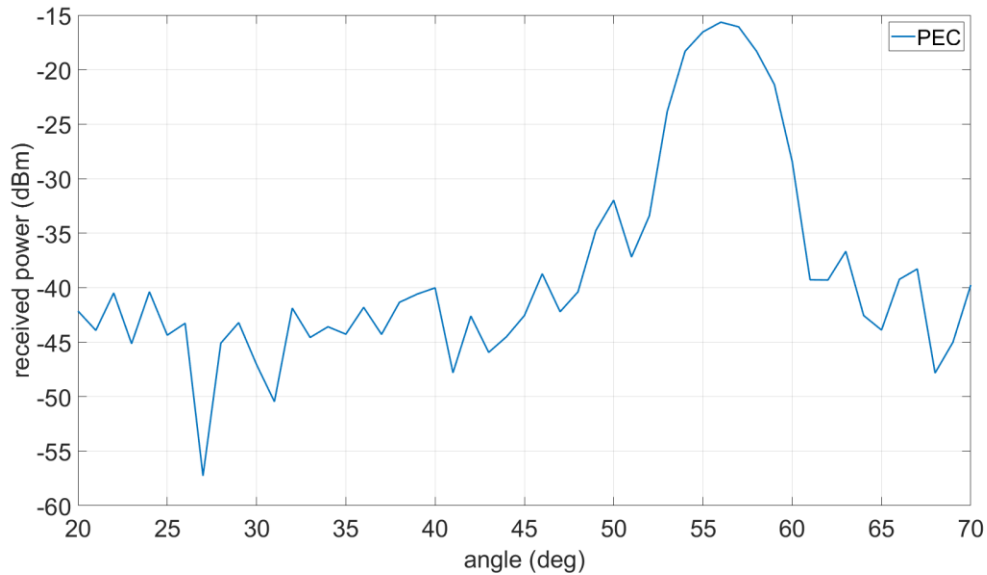
Figure 2.17: Bistatic Measurement Result for PEC Facing 30 Degrees (Measured Every 1°)

These results are for the first prototype of the RIS which is physically curved towards one side. Figure 2.15 shows the differences between the RIS's RCS pattern when it is by itself, mounted to the control board, and when spacers are put between the RIS and the control board. The RIS becomes flat when it is mounted on the control board. This could explain the difference in max power level between the different configurations although it is only 1.6 dB at most. The measurement setup can clearly resolve the main beam, but it does not seem to be able to resolve the sidelobes clearly. It was discovered that the lens was reflecting some of the signal from the Tx antenna and it was likely causing enough multipath interference in the measurement to impact the sidelobes. Changing the frequency of operation for the RIS didn't seem to impact the max power level much but it did change the sidelobes. The difference in max power level of the RIS and the PEC is now 8.38 dB which is about the same compared the previous setup. However, the setup used in the final measurement was a lot easier to align and more

28

reliable. The 8.38 dB loss was still higher than expected but this seemed to be a flaw with the RIS rather than the measurement setup. 3 dB of loss is accounted by the quantization lobe. There are additional losses due to surface waves, dielectric, and conductor loss but they should not be high enough to cause this difference.
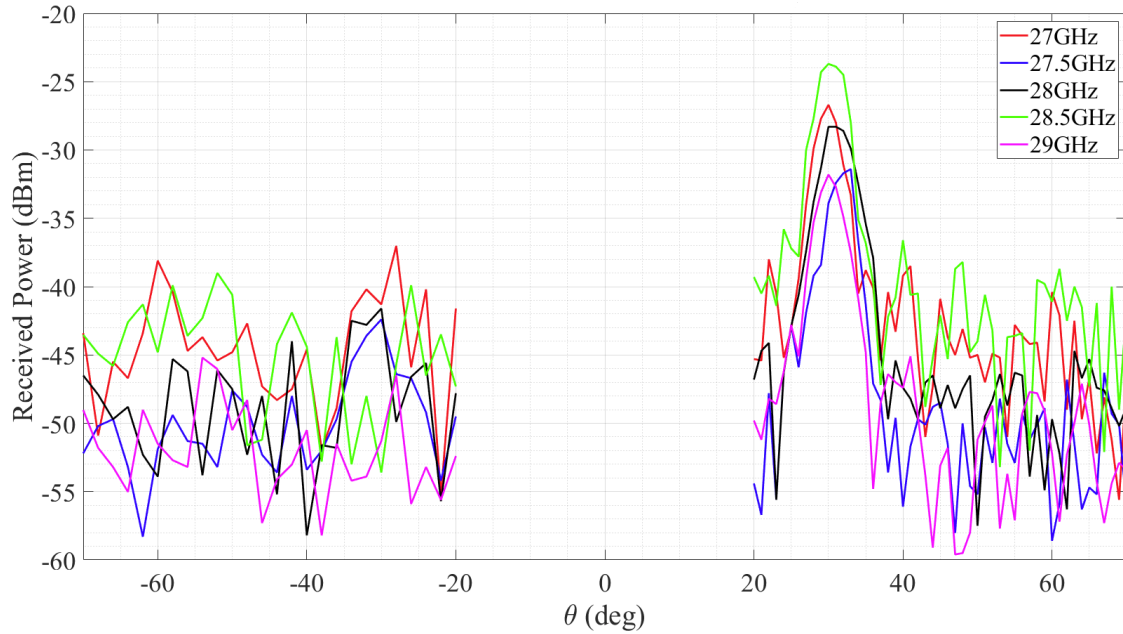

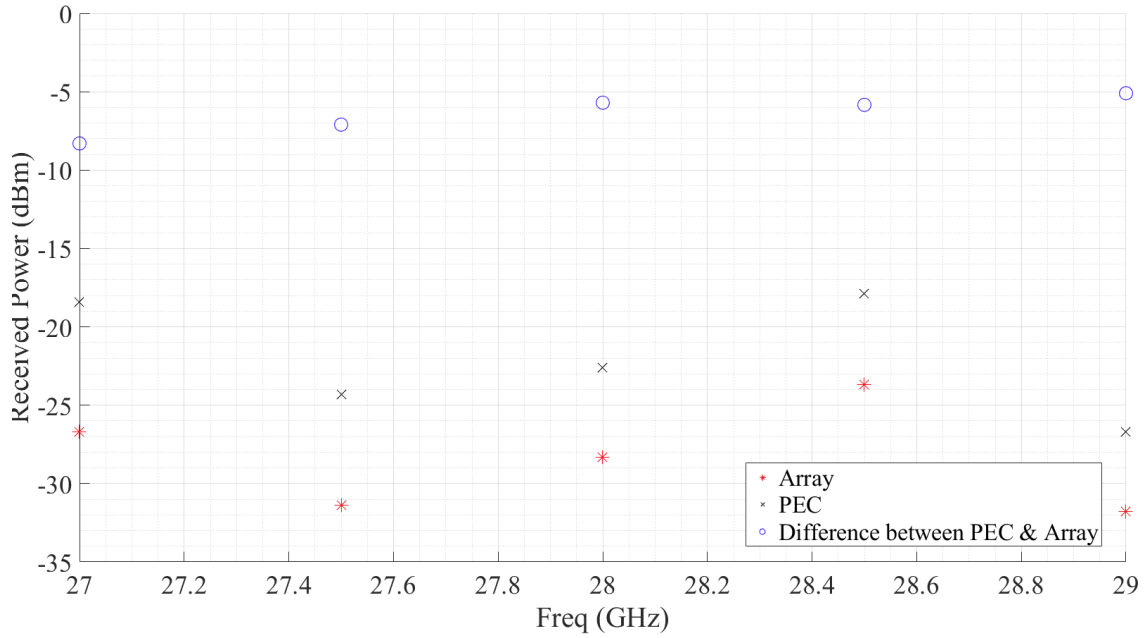*Figure 2.18: RCS Pattern for New RIS at Different Frequencies*

Figure 2.19: Comparing Max Received Power Between RIS and PEC

The new version of the RIS is flat unlike the previous version which is physically curved to one side. Measurement results for the new RIS are shown in figure 2.18 and 2.19. The difference between the max received power of the RIS and the PEC is now at 5.84 dB (at 28.5 GHz) whereas the old version of the RIS used to be at 8.38 dB. This indicates the new version of the RIS has much lower losses.

CHAPTER 3

MONOSTATIC SETUP TO FIND SIDELOBE AT BORESIGHT

Setup Iteration

It was suspected that a large sidelobe was present at or near 0 degrees. The bistatic measurement setup would not be able to identify it because the lens and Tx antenna would block line of sight to the Rx antenna. A monostatic measurement setup was needed to find this sidelobe.
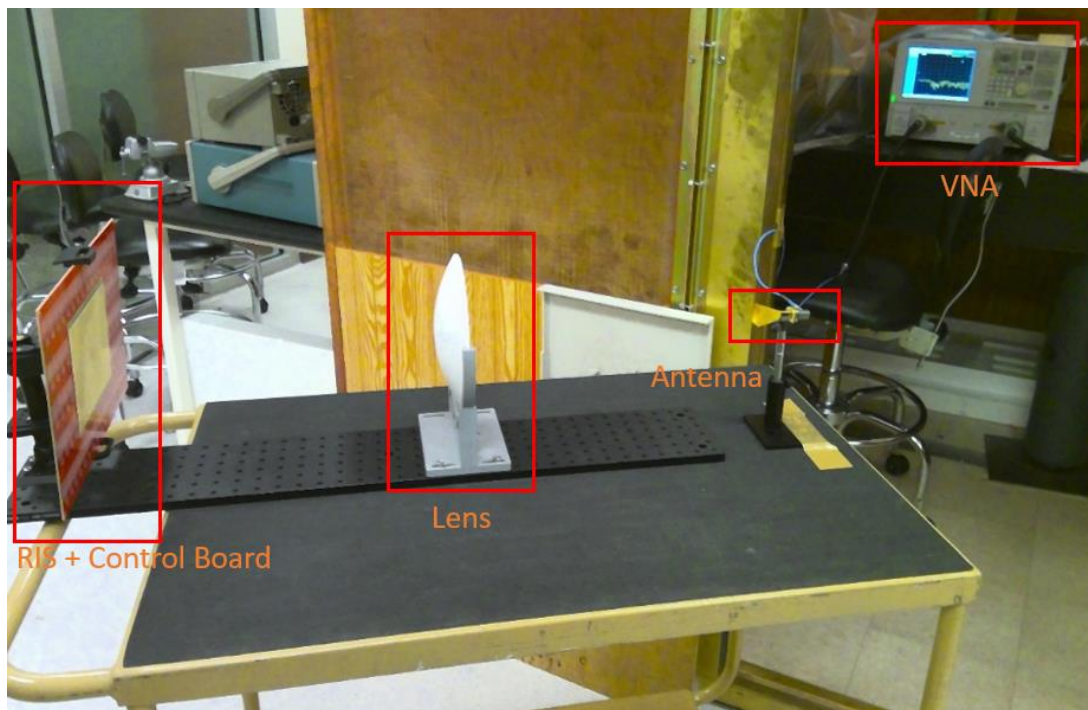

Figure 3.1: Preliminary Monostatic Measurement Setup

This setup borrows many parts from the bistatic measurement setup such as the adjustable angle plate, tablet holder, lens, and antenna fixture. It is a simpler setup compared to the bistatic setup. The antenna is connected straight to a VNA. There is no

need to use the upconverter/downconverter since the VNA works up to 40 GHz. Similar

to the bistatic measurement, a PEC needs to be measured to provide a reference for the

measurement results. The RIS or PEC was placed 45 cm away from the lens.
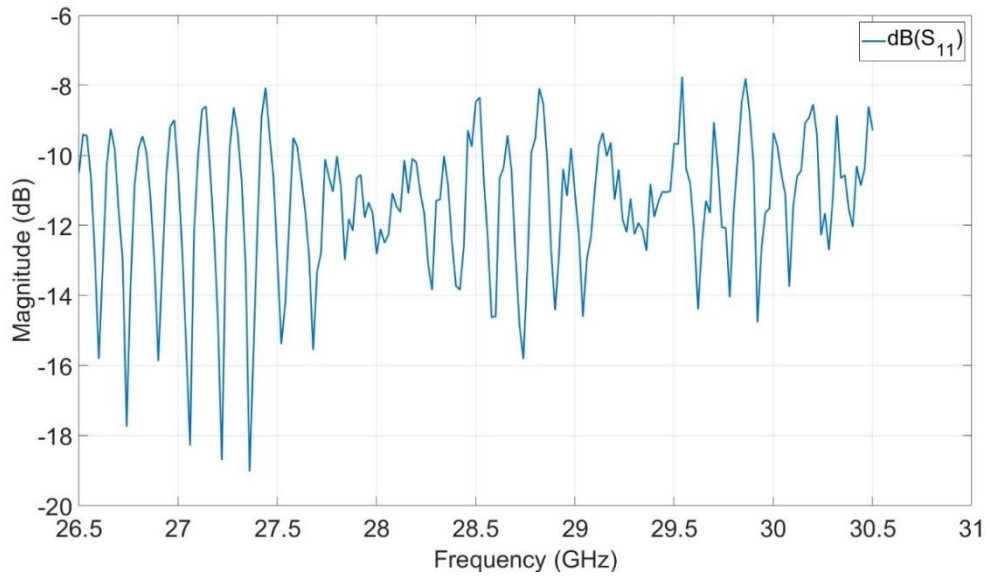

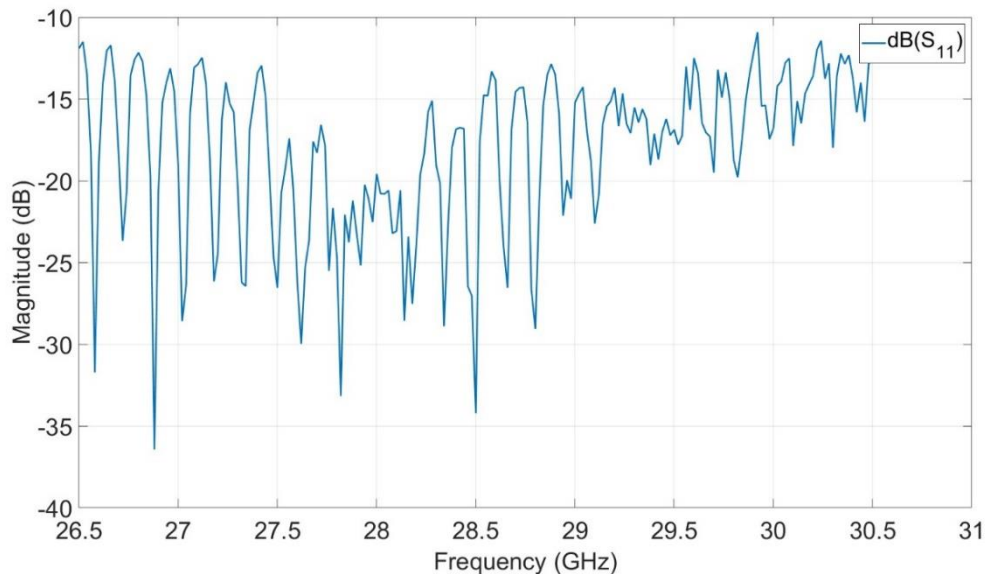*Figure 3.2: Monostatic PEC S11 Measurement (No Time Gating)*

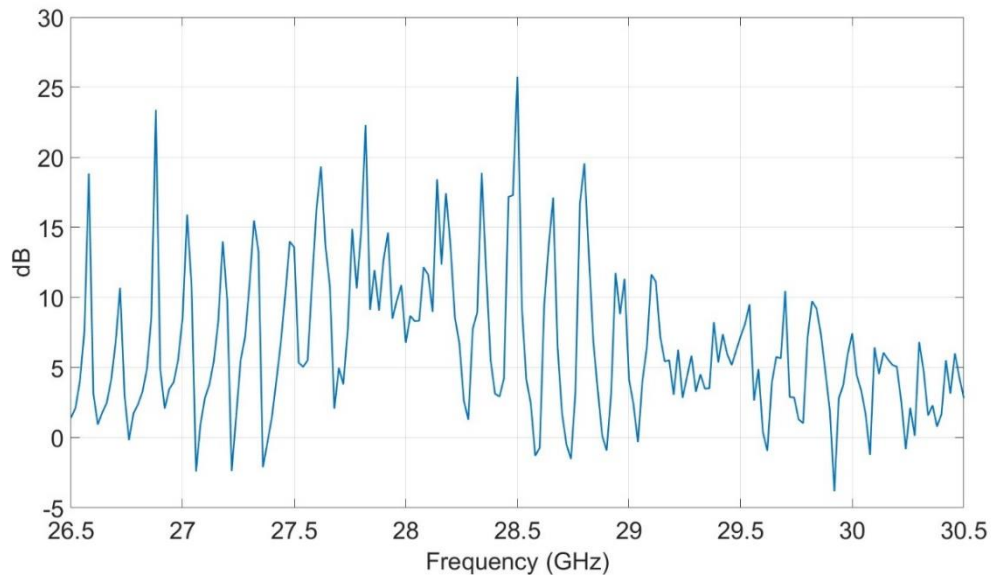*Figure 3.3: Monostatic RIS S11 Measurement (No Time Gating)*

Figure 3.4: S11 Difference Between PEC and RIS Without Time Gating. Positive Value Means S11 of PEC is Higher than RIS
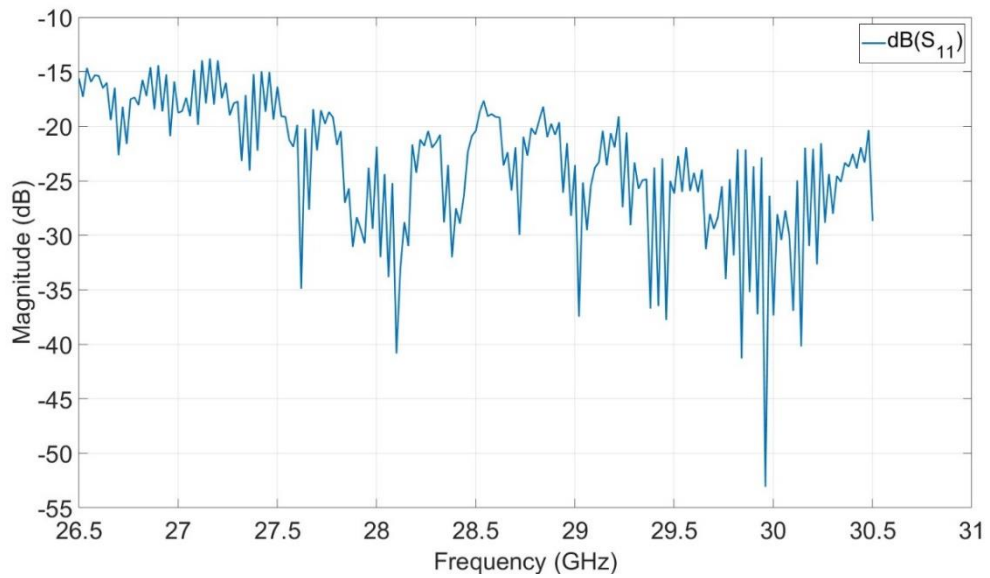

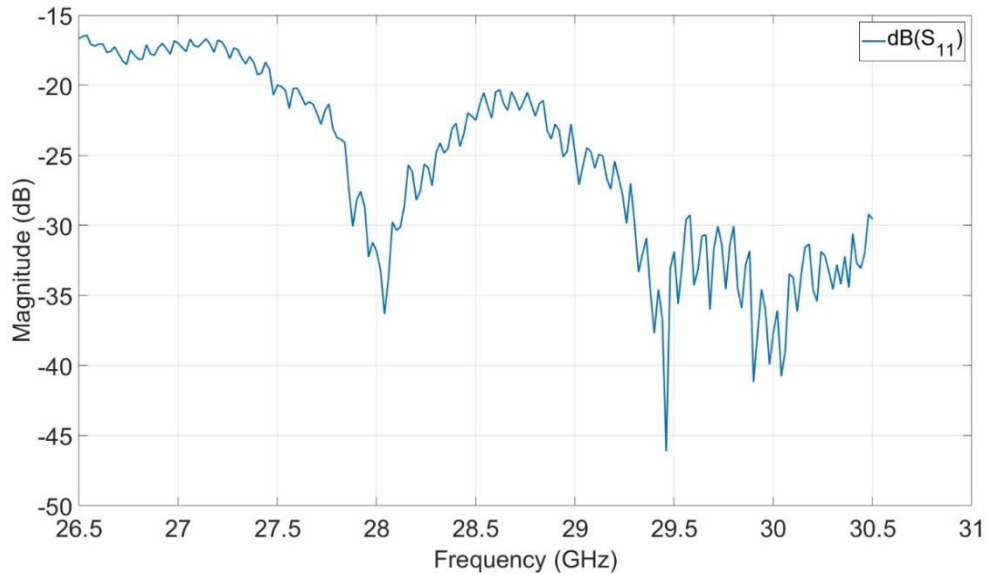*Figure 3.5: Monostatic S11 Measurement with Only Lens*

Figure 3.6: Measured S11 of Horn Antenna

These S11 plots show how much of the signal is reflected back to the VNA through the antenna. There is many sharp ringing across the frequency range which is an unexpected behavior. In figure 3.2, taking the difference between the S11 of the PEC and RIS still shows this ringing behavior. Something in the setup must not be configured correctly for the difference between the PEC and RIS to change so drastically across the frequency. The S11 with only the lens also has sharp variations which show that the lens might be causing the issue. There is ringing in the S11 of the horn antenna but that is caused by the calibration kit and is much smaller than the ringing observed in other S11 plots.

Figure 3.7: Attempted Monostatic Measurement Setup Without Lens

There was suspicion that the lens was causing issues with the measurement. An attempt at measurement was done without the lens. The distance of the PEC from the antenna was varied from 5 meters to 90 cm but there was no change to the S11 plot compared to the S11 of the antenna itself. Without the collimating lens, the S11 was dominated by the S11 of the antenna because not enough power arrived at the antenna.

Experimenting with the lens position in lab and HFSS simulations show that the lens was indeed causing the huge variations in S11. More specifically, the lens was reflecting some of the signal instead of completely passing it through.
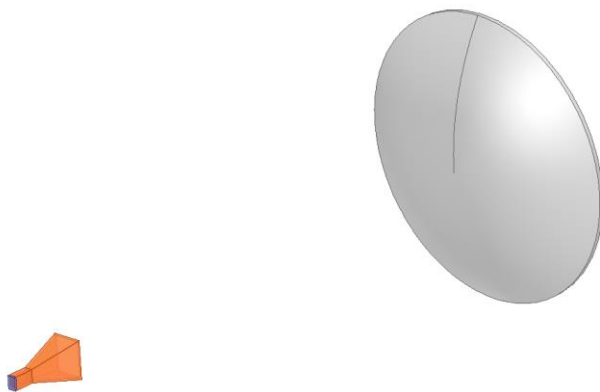

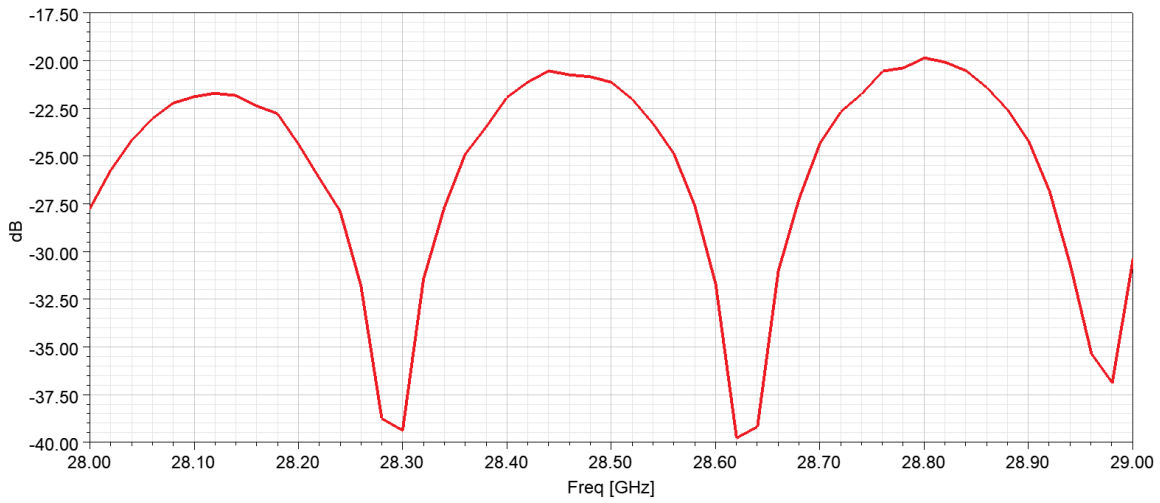*Figure 3.8: HFSS Setup for Simulating Antenna and Lens*
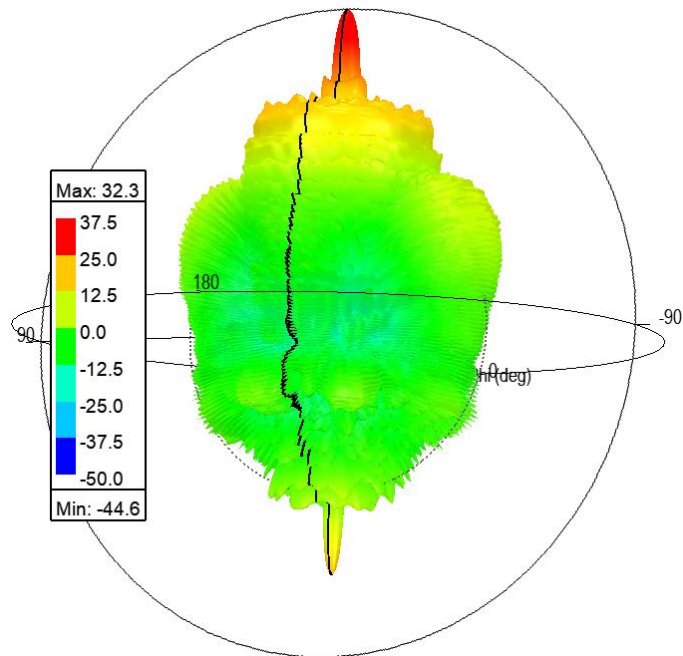
Figure 3.9: HFSS S11 Plot at Antenna Port

Figure 3.10: Gain Plot of Far-Field Radiation for Horn Antenna and Lens Setup
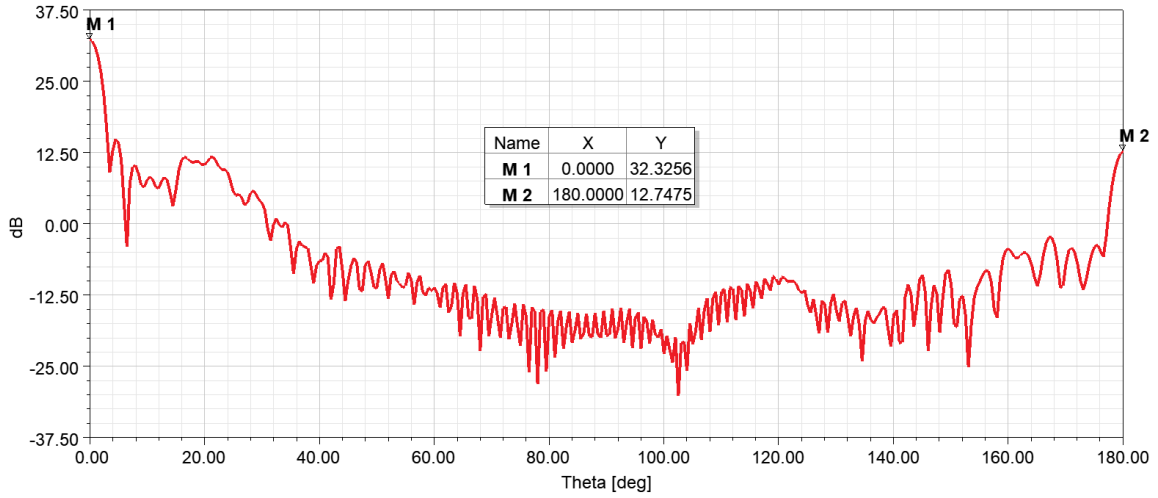
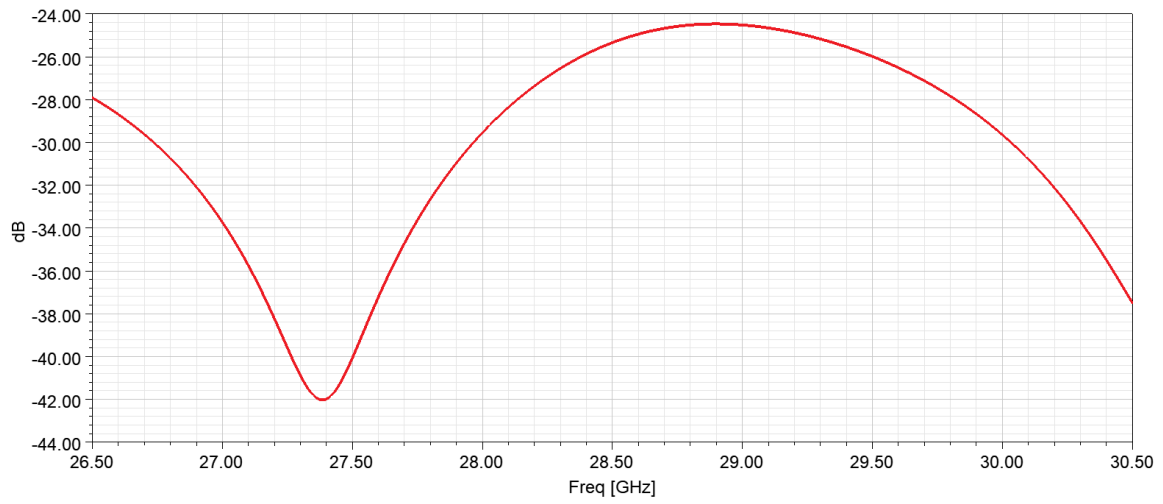*Figure 3.11: Phi = 180° Cut of Far-Field Gain Plot*

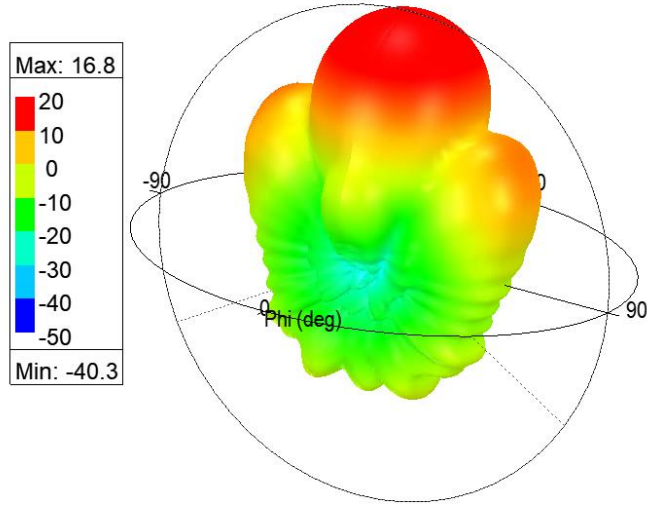*Figure 3.12: Return Loss of Horn Antenna Simulated in HFSS*

Figure 3.13: Far-Field Gain Plot of Horn Antenna Simulated in HFSS

HFSS simulation was done using FE-BI hybrid region. Figure 3.9 shows that there is a large variation in S11 even over a small frequency range of 28 GHz to 29 GHz. The gain plot and its phi=180° plane cut show that there is significant back lobe for the antenna + lens setup; as high as 12.75 dB. While it is about 20 dB less than the front lobe, the directivity is comparable to the horn antenna by itself which has a gain of 16.8 dB in simulations (15 dB according to spec sheet). The S11 of the antenna by itself is also relatively constant from 28 GHz to 29 GHz so it is not an inherent problem with the antenna.

Using time gating is a viable way of removing unwanted reflections back to the antenna [13]. Time gating can be done on the VNA itself. The VNA shows the distance between the end of the cable (point where VNA is calibrated) to the RIS which confirms that this reflection is caused by the RIS.

$$Time\ domain\ resolution\ distance: \Delta d = \frac{2c}{BW} = 4.44\ cm \qquad (5)$$

38

There needs to be enough bandwidth in the measurement for enough resolution to differentiate reflections caused by different objects in the setup. To be safe, the VNA was made to measure from 26.5 GHz to 40 GHz which gives a resolution distance of 4.44 cm.
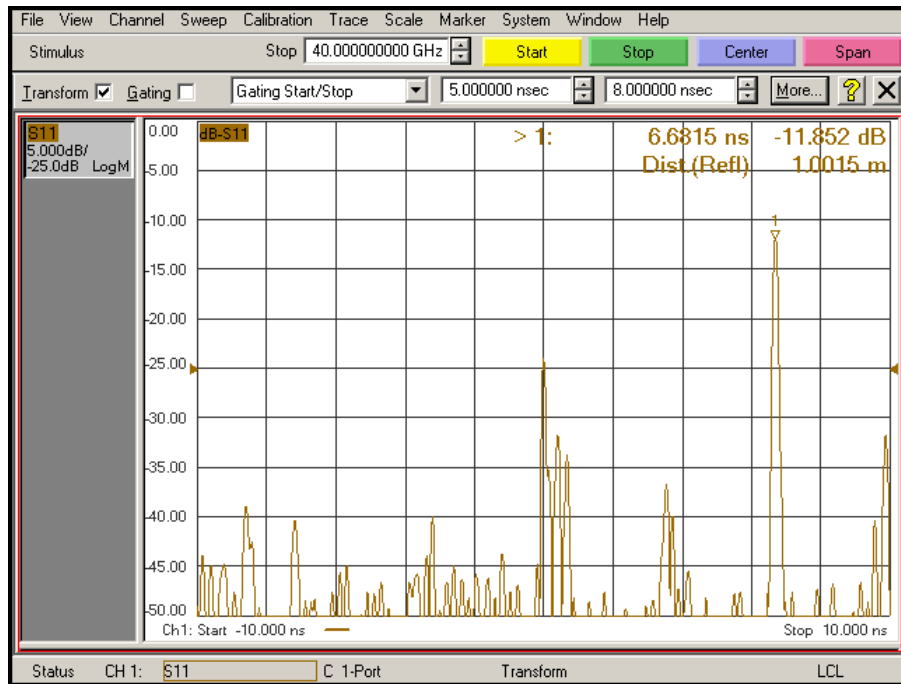

Figure 3.14: S11 Transformation to Time Domain on VNA Without Time Gating

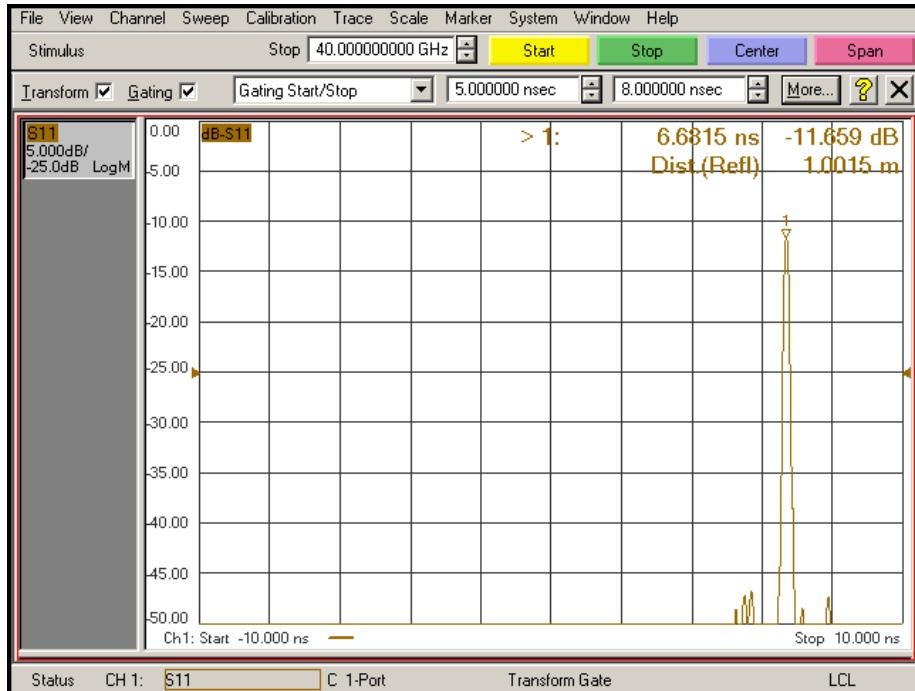*Figure 3.15: S11 Transformation to Time Domain on VNA With Time Gating*

Sharp distinct signals can be seen in the time domain plot because of the

exceptional resolution that was used. It can be seen from figure 3.14 that there are a lot of

unwanted reflections that were picked up by the VNA. Applying the time gating removes

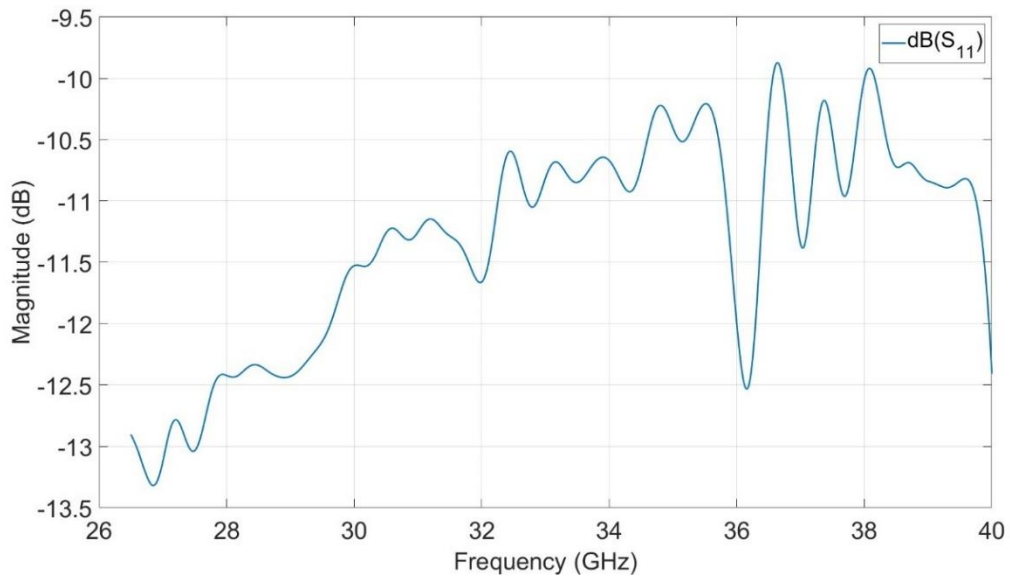nearly all the other unwanted reflections from the S11 measurement as seen in figure

3.15.

Figure 3.16: S11 of PEC at 45 cm Away from Lens (Time Gated)
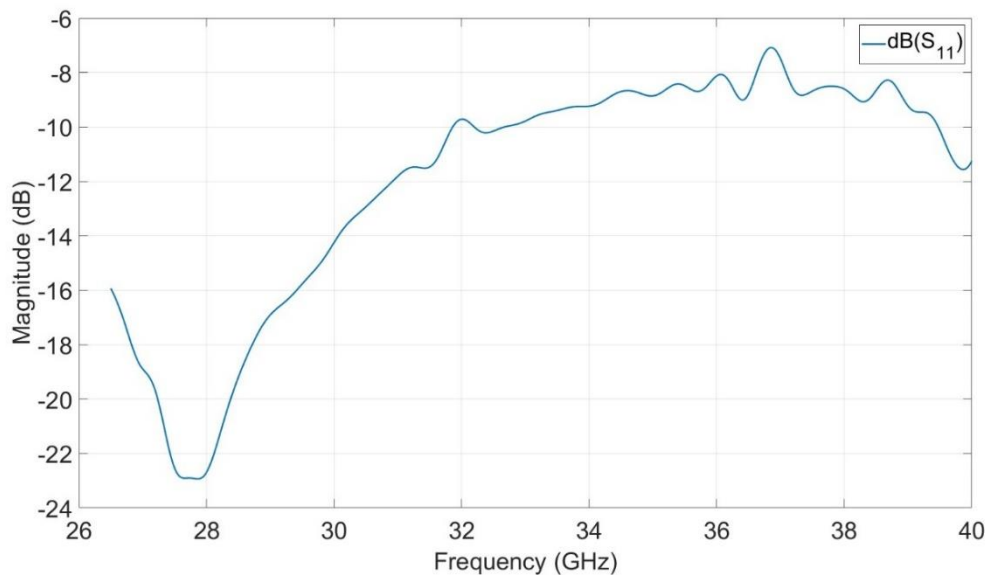
Figure 3.17: S11 of RIS at 45 cm Away from Lens (Time Gated)

41
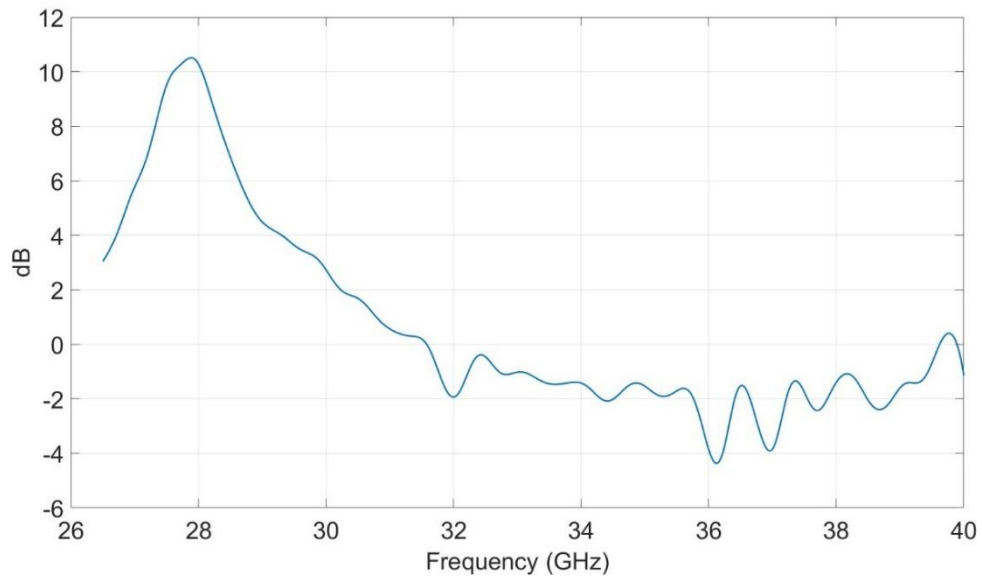
Figure 3.18: S11 Difference Between PEC and RIS After Time Gating (45 cm from Lens)

After applying time gating, the S11 is much more stable. Taking the difference in S11 between the PEC and RIS now gives a clear trend. However, the plot goes to negative values for some frequencies meaning that the S11 of the RIS is larger than for the PEC. The S11 of the PEC should always be larger than for the RIS because it is an ideal mirror. Some changes were made to the setup to resolve this issue.

Figure 3.19: Modified Fixture for Monostatic Measurement Setup

The fixture has been modified to allow for alignment in the yaw axis and pitch axis whereas the previous fixture only allowed alignment in the pitch axis. There was no need for this in the bistatic measurement setup because the Tx antenna was swept along this axis anyway. With this change, the alignment is more accurate for maximum reflected power.
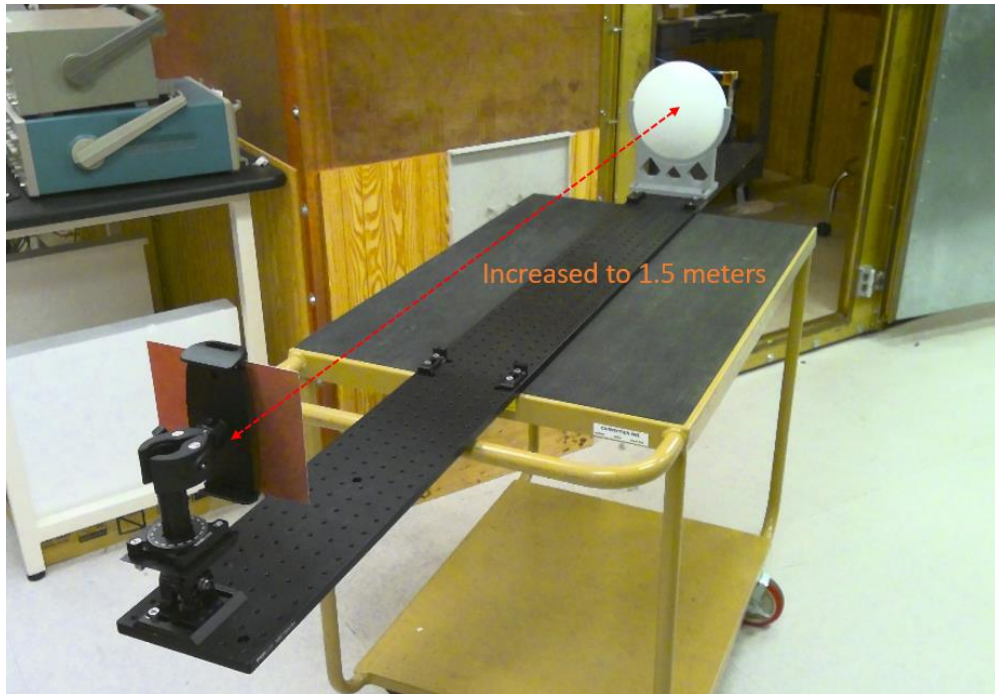
Figure 3.20: Fixture Placed 1.5 Meters Away from Lens

The distance of the measured object from the lens affected the difference in S11 between the RIS and PEC. As the fixture was placed further away, the S11 of the PEC rises (in absolute terms, not just compared to S11 of RIS) until the S11 of the PEC is higher than the RIS for all frequency ranges. The same pattern happens for the RIS mounted on the control board where the S11 increases relative to the RIS by itself. The RIS is curved while the PEC and RIS mounted on the control board was flat. From this it can be concluded that there are issues with the phase of the illumination at different distances from the lens. By experimenting with the distances in the lab, it was observed that a distance of 1.5 meters away from the lens gave the best result. In this case, best result means that the difference between PEC and RIS mounted on the control board to the RIS by itself was the largest.
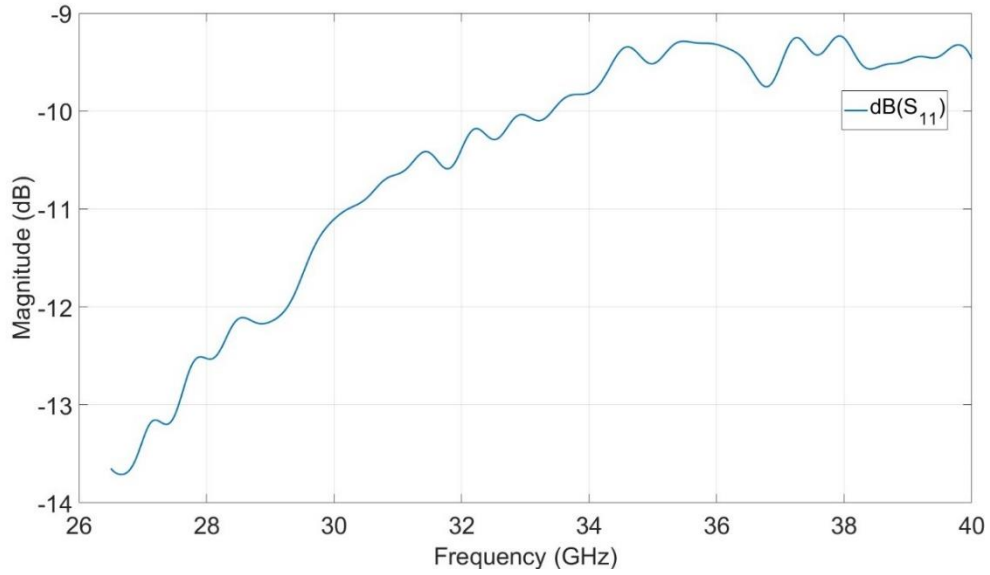
Final Measurement Result

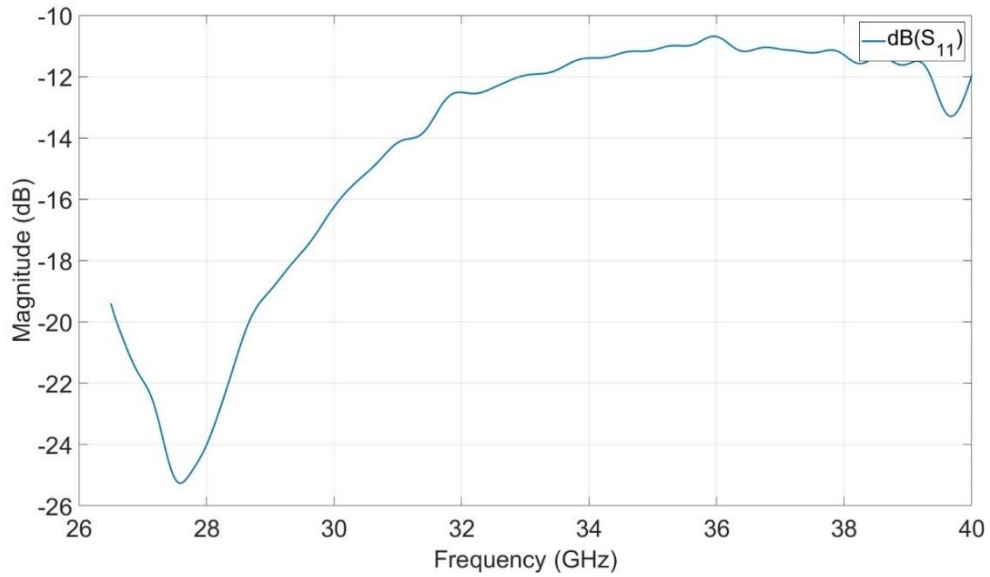*Figure 3.21: S11 of PEC at 1.5m Away from Lens (Time Gated)*

Figure 3.22: S11 of RIS at 1.5m Away from Lens (Time Gated)
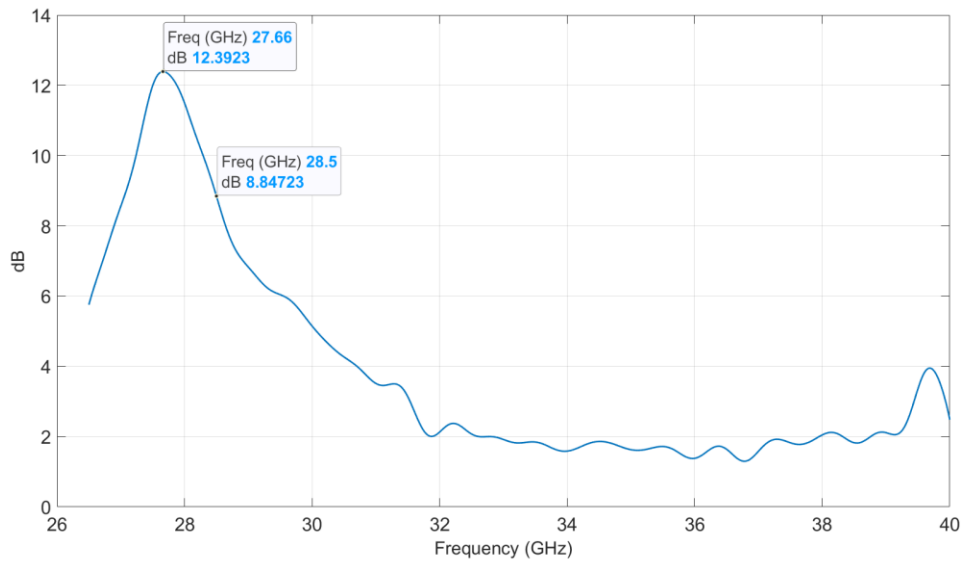
Figure 3.23: S11 Difference Between PEC and RIS (Final Measurement)

Figure 3.24: S11 Difference Between PEC and RIS + Control Board (With Spacer) (Final Measurement)
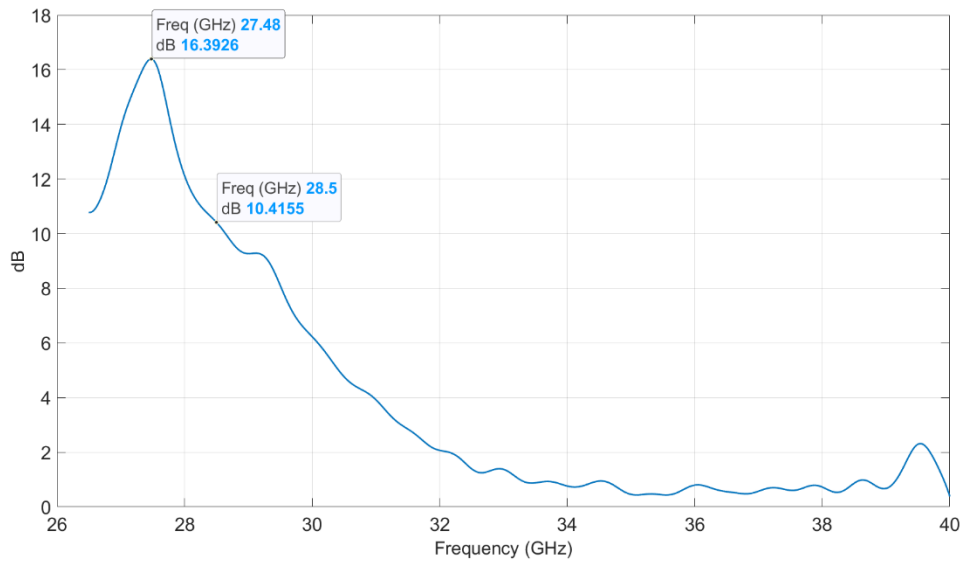
Figure 3.25: S11 Difference Between PEC and RIS + Control Board (No Spacer) (Final Measurement)

These results are for the RIS at 1.5 meters away from the lens. There is a much smaller sidelobe at the boresight when the RIS is operating around 27.6 GHz. This implies that this copy of the RIS works best at 27.6 GHz instead of the design frequency of 28.5 GHz. The sidelobe is smallest with the 'RIS + control board (no spacer)' configuration. In figure 3.25, the marker at the peak shows 16.4 dB meaning that the sidelobe for the RIS at 0 degree is 16.4 dB less compared to the PEC. Recall that the main lobe of the RIS (at 30°) was found to be 8.38 dB less than the PEC. In best case scenario, the sidelobe at 0 degrees is only 8 dB less than the main lobe for the RIS.
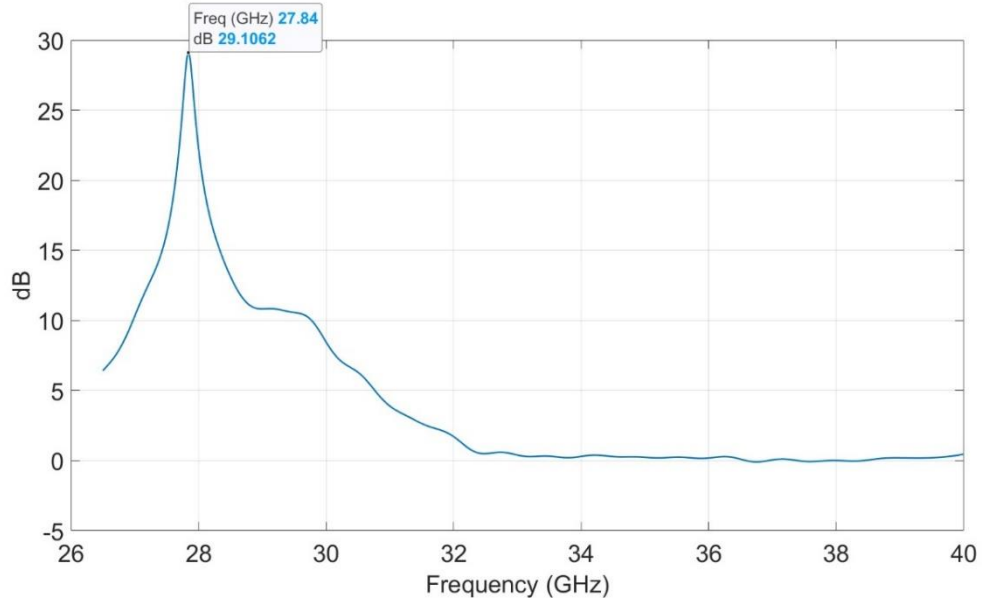
Figure 3.26: S11 Difference Between PEC and New Version of RIS (Time Gated)
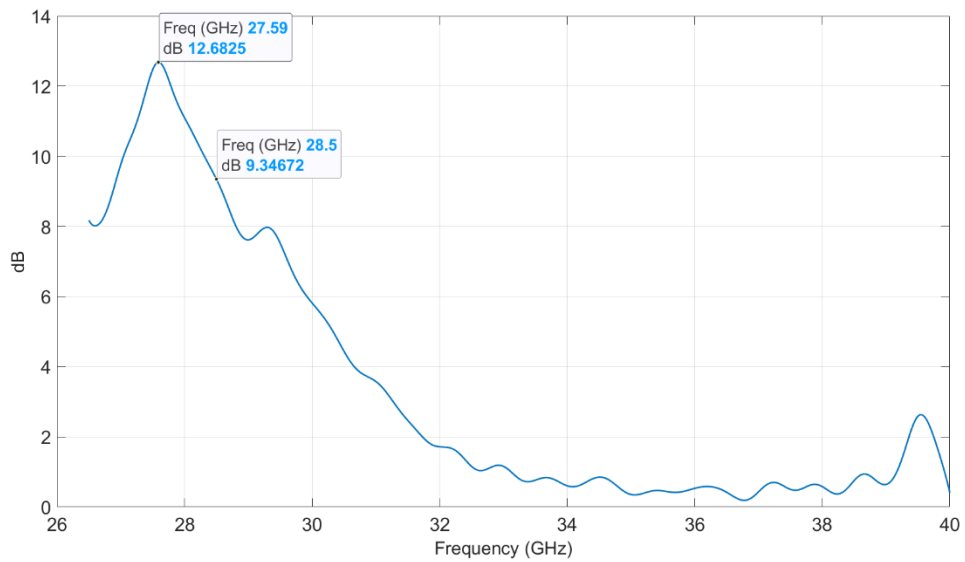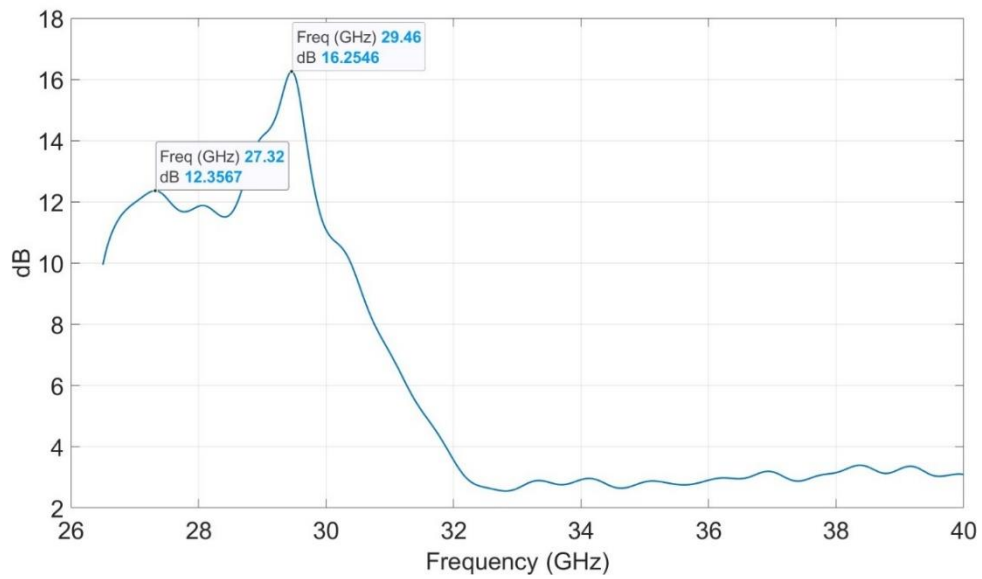

Figure 3.27: S11 Difference Between PEC and New RIS + Control Board (No Spacer)
(Time Gated)
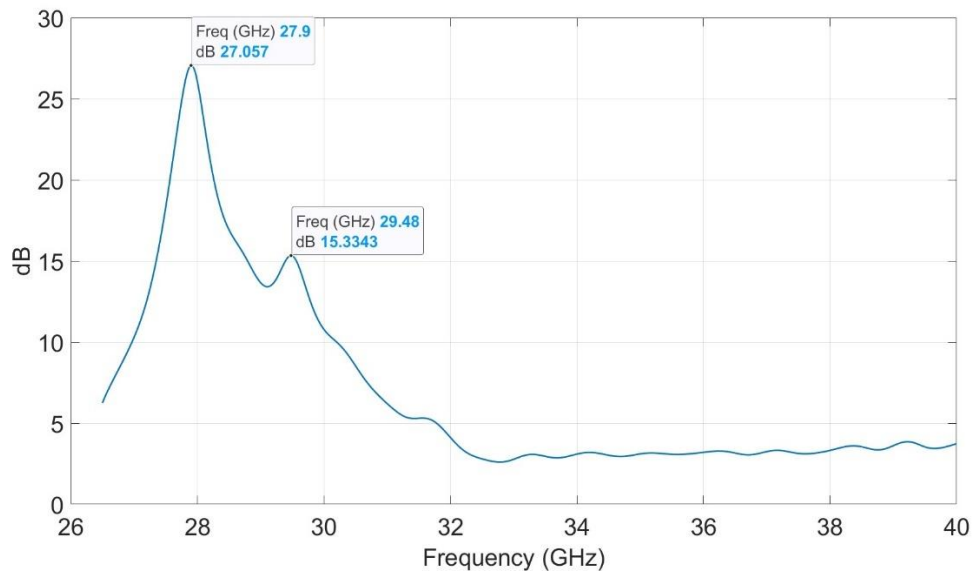
Figure 3.28: S11 Difference Between PEC and New RIS + Control Board (With Spacer)
(Time Gated)

The plots show the measurements for the new version of the RIS. The sidelobe at boresight is vastly improved compared to the old version of the RIS. It is now about 22 dB down from the main lobe when the frequency of operation is around 27.9 GHz and still performs decently over a narrow frequency band.

CHAPTER 4

COMPARISON OF MEASUREMENT TO ANALYTICAL RESULT

Simulation Setup

In actual applications and in the design of the RIS, it was assumed that a uniform plane wave (or something close to it) would impinge on the surface of the RIS. It was calculated previously that the far-field region of the RIS is further than 5.36 meters and the devices that would interact with the RIS in actual application would be much further than that. The measurement setup in lab is evaluated to see how much it deviates from the ideal uniform plane wave and what effect it has on the RCS pattern of the RIS.

Figure 4.1 shows the measurement setup in lab being recreated in HFSS. The actual RIS with 25x32 elements would be too large to simulate so a sheet with the same dimensions as the RIS was used in its place. There would also be no point to simulate the unit cell for the purpose of this thesis since it would not include the effects of the measurement setup. This simulation finds out the amplitude and phase of the impinging E-field on the RIS.
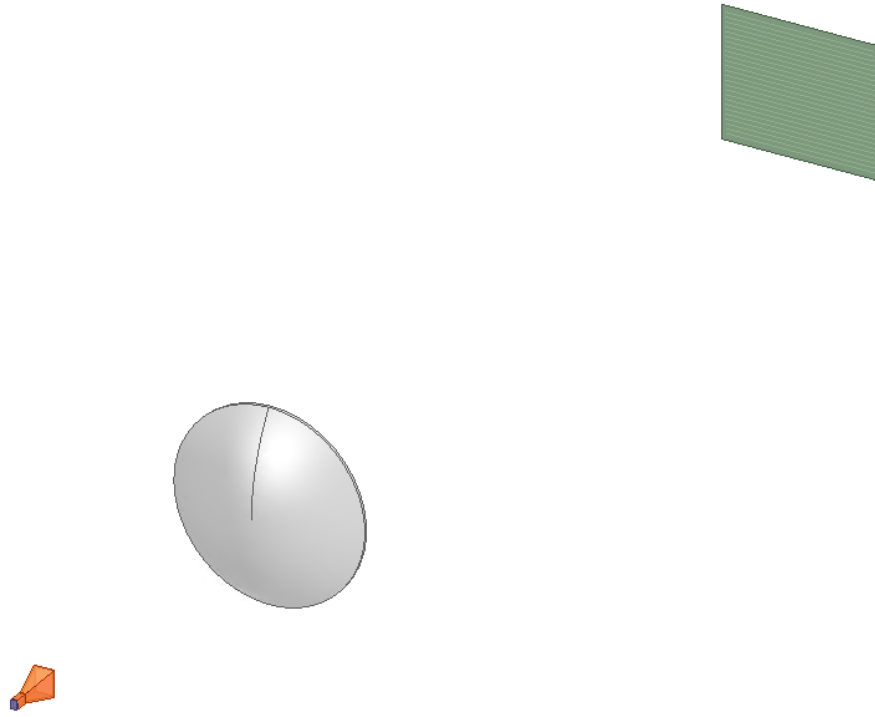
Figure 4.1: HFSS Setup to See E-Field Projection on RIS

Simulation Result
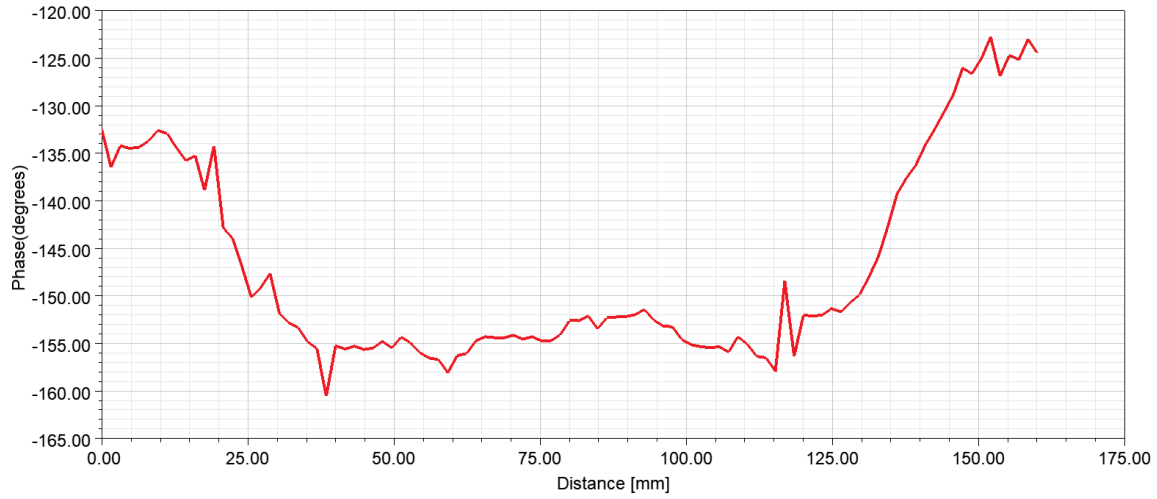
Figure 4.2: Illumination Phase on RIS at 90 cm from the Lens
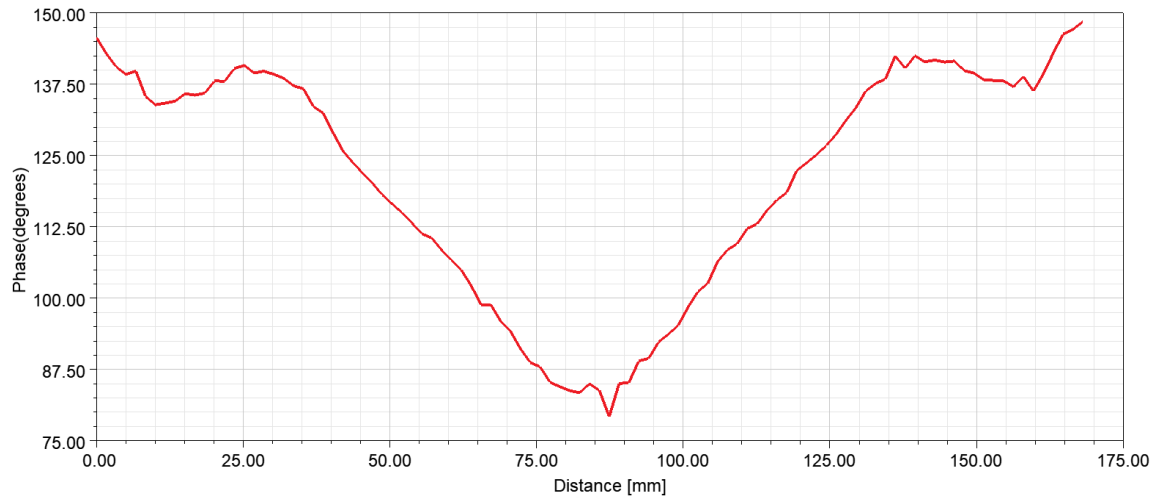
Figure 4.3: Illumination Phase on RIS at 45 cm from the Lens
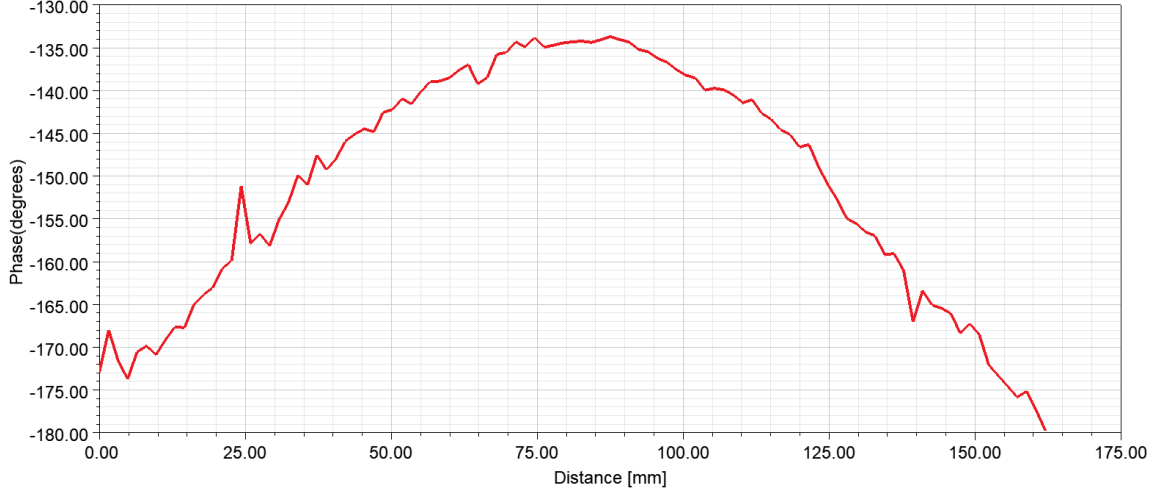
Figure 4.4: Illumination Phase on RIS at 1.5 Meters from the Lens

Simulation results for the measurement setup in HFSS show that the illumination phase on the RIS varies a lot with distance from the lens. The distance on the x-axis of the plot refers to the lengthwise position on the RIS. Ideally, there should a plane wave by the time the radiation reaches the RIS. There is a huge change in phase across the RIS when it is placed 45 cm away from the lens which explains why the monostatic measurement at 45 cm had unexpected results. At 90 cm away from the lens, the phase is relatively constant near the center of the RIS and tapers at the edge. Looking at figure 4.5, most of the radiation is concentrated near the center of the RIS board so the change in phase near the edges is not too concerning. A phase error of less than 22.5° does not impact the analytical solutions by much [14]. The derivation for the far-field region assumes a max phase error of $\frac{\pi}{8}$.

$$Far-field\ max\ phase\ error = \frac{k \cdot \left(\frac{D}{2}\right)^2}{2r} \leq \frac{\pi}{8} = 22.5° \qquad (6)$$

53

This shows that any deviations in the RCS pattern of the RIS compared to the analytical solutions are mainly caused by the non-uniform amplitude. The bistatic measurement was performed at 95 cm from the lens which is close to the 90 cm used in the simulation. The same can be said for the simulation at 1.5 m (used in monostatic measurement) from the lens where the phase does not deviate more than 22.5° unless it approaches the edge of the RIS board, at which point the amplitude of the impinging E-field has tapered off significantly.

Figure 4.5: E-Field Amplitude Projection for RIS at 45 cm, 90 cm, and 1.5 m Away from Lens

There are 3 main factors that can affect antenna measurements; they are transverse amplitude taper, longitudinal amplitude taper, and phase variation. It is
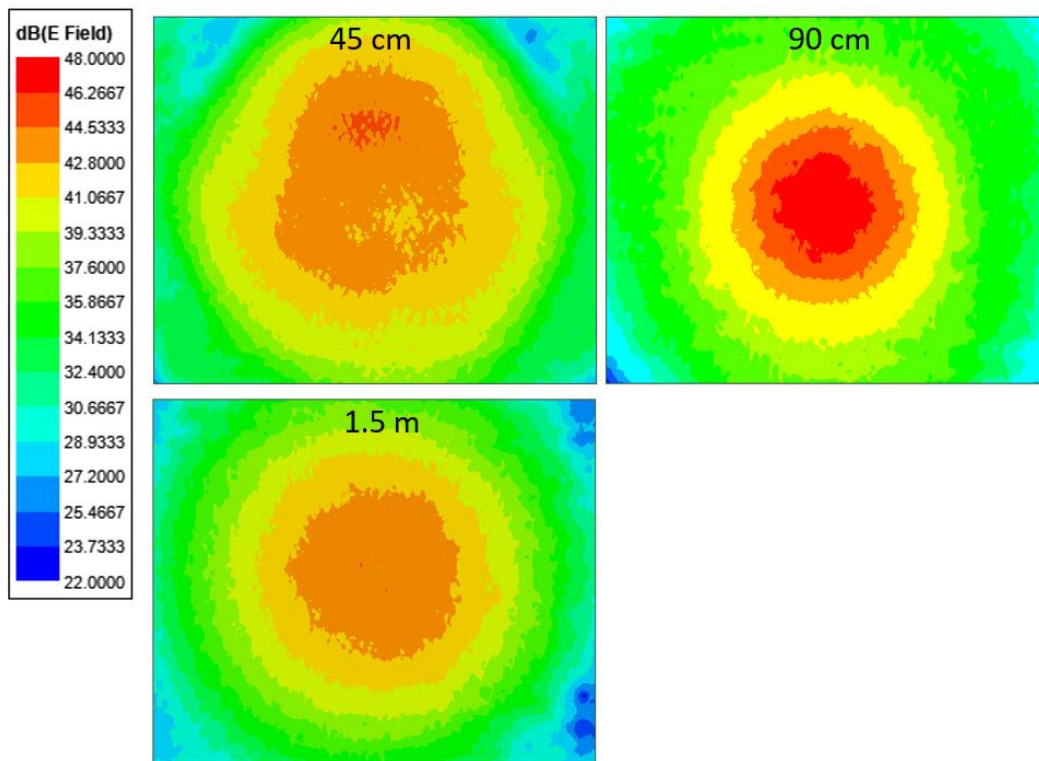
generally recommended to use a 0.25 dB taper over the test aperture [15]. Figure 4.5 show that the transverse amplitude taper is about 10 dB. An amplitude tapering this large will reduce the gain of the main beam. It is not a problem in this case because the power level is referenced to the max received power with the PEC which will also go down along with the RIS power level. However, the sidelobe level (SLL) will appear lower than it should be when there is an amplitude taper and there will not be clear nulls between the sidelobes. This is one of the reasons why the measured RCS pattern did not show clear sidelobes.

The longitudinal amplitude taper refers to the taper along the range of the antenna. This is usually only a concern for high gain end-fire antennas that are lengthy along the range axis. Many antennas like the horn antenna can have its radiation pattern approximated as a gaussian beam. A gaussian beam has a transverse variation that is much larger compared to the variation along the axis.

$$\frac{\partial u}{\partial z} \ll \frac{\partial u}{\partial x} \ and \ \frac{\partial u}{\partial z} \ll \frac{\partial u}{\partial y} \tag{7}$$

$$where \ E(x, y, z) = u(x, y, z)e^{-jkz}$$

The simulation results show that this holds true since the magnitude of the E-field barely changes at 45 cm, 90 cm, and 1.5 m away from the lens. Meanwhile the magnitude of the E-field changes drastically away from the center of the RIS whether it is in the X or Y direction. Thus, the longitudinal amplitude taper is not of concern.

It was stated previously that the phase along the RIS was constant enough to be considered in the far field at 90 cm and 1.5 m away from the lens. When the antenna is at

the focal point of the lens, the spherical wave from the antenna is turned into a plane wave. It shares the same concept and characteristics as a reflector used in a Compact Antenna Test Range (CATR). The field produced by a reflector is not a perfect uniform plane wave because of its finite size and surface imperfections. Only a portion of the fields consists of nearly planar wavefronts, and this is referred to as the "quiet zone" [14]. The amplitude also decreases rapidly outside of the quiet zone. Figure 4.2 illustrates this concept well where the phase is relatively constant from 30 mm to 125 mm and quickly changes outside of that range. Phase ripples inside the quiet zone is caused by diffraction at the edge of the lens.

The focal length of the lens needs to be given a closer look. If the focal length of the lens was indeed 44.5 cm, then the phase should be most uniform at 44.5 cm away from the lens. This did not seem to be the case based on the simulation results.

Finding Analytical RCS Pattern

A MATLAB code that calculates the array factor of the RIS was used as the comparison to the measured RCS pattern. In this context, array factor and RCS pattern can be used interchangeably. In the code, it was assumed that the impinging radiation is a plane wave with constant amplitude and phase. To get analytical results that are closer to what was expected from the measurement, the amplitude and phase information from the measurement setup in HFSS needs to be exported to MATLAB.

Sampling ($\vec{E} \cdot \vec{u}$) along each line.
$\vec{u}$ = unit vector tangent to the line
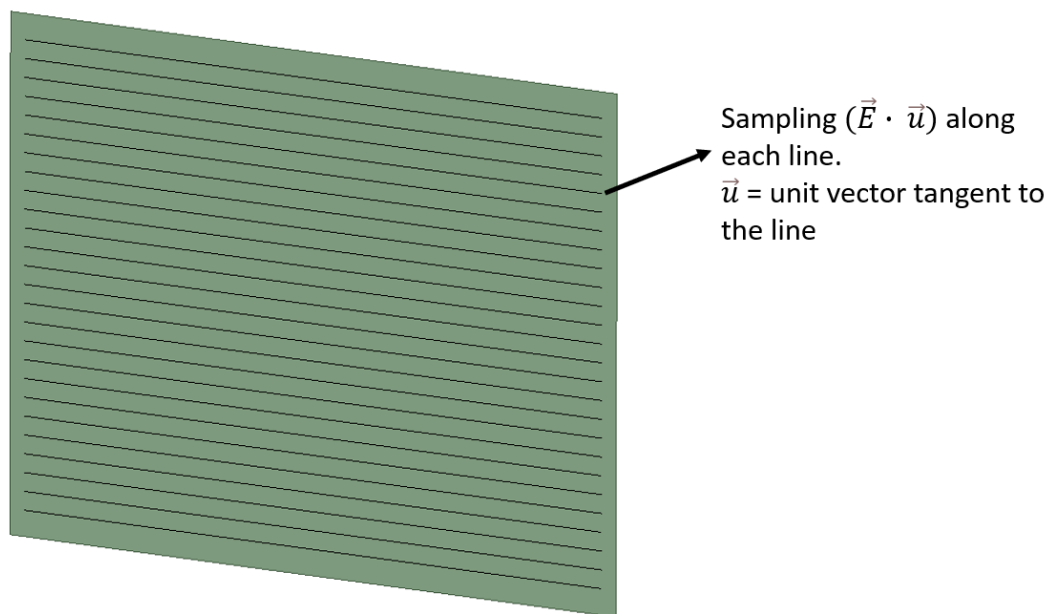
Figure 4.6: Lines on a Surface with Same Dimensions as the RIS Used to Sample Amplitude and Phase

The simulation setup is the same as in figure 4.1. All the steps outlined here are just post-processing. Non-model lines are added to the surface to be used for sampling. An expression for sampling the phase and amplitude were made using the fields

57

calculator in HFSS. Using these expressions, you can plot the values for either phase or amplitude along the line with a certain number of points. In this case, use the number of elements along the row of the RIS as the number of points in the plot which would be 32 points. Instead of creating a rectangular plot, it would be better to display the data as a table for each row. There would be 25 tables in total of size 1x32. Combine these tables into one whole table of size 25x32 and export as a csv file to be used in the MATLAB code.
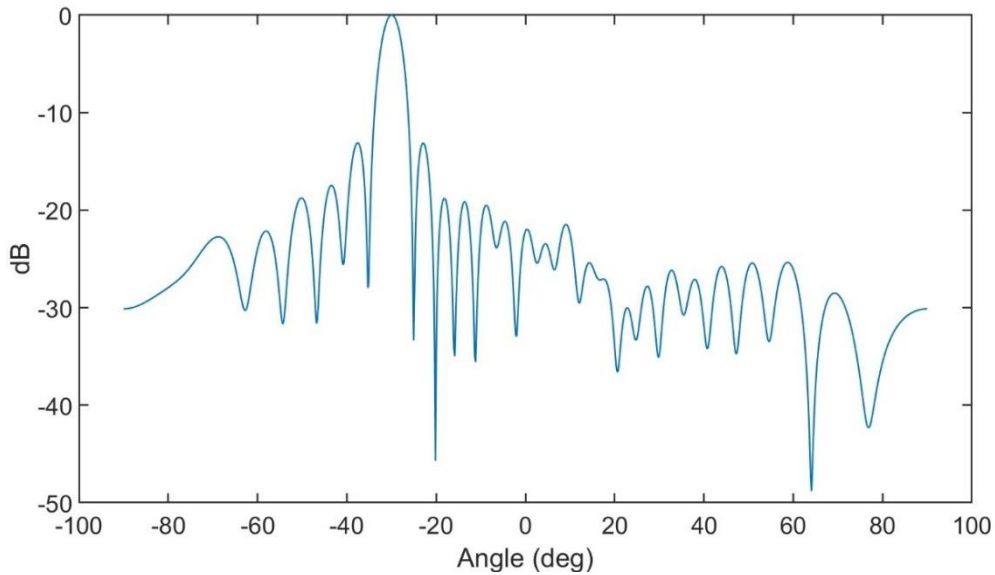
Figure 4.7: MATLAB Array Factor (Plane Wave Illumination)
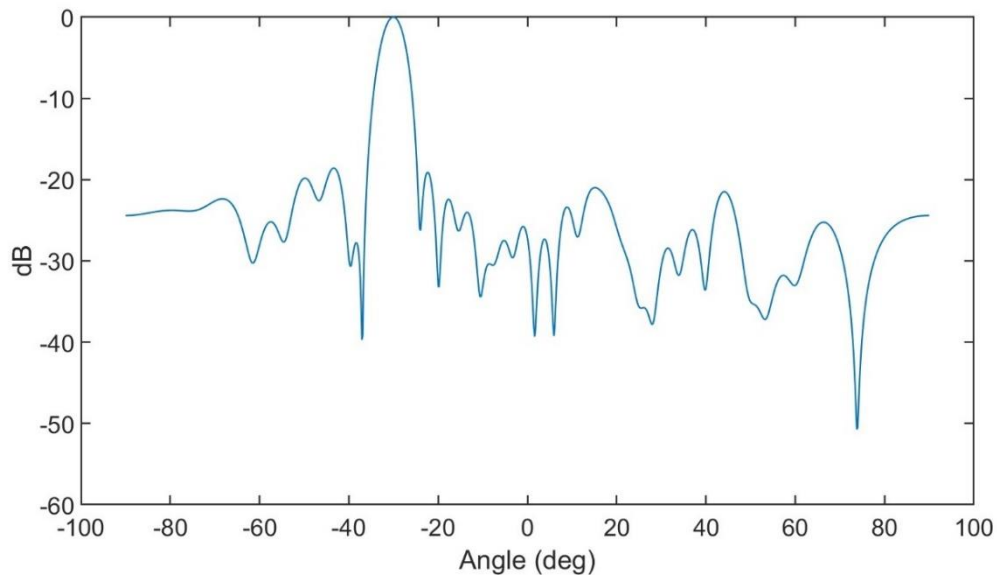
Figure 4.8: MATLAB Array Factor (Imported Illumination from HFSS Using 90 cm Distance)
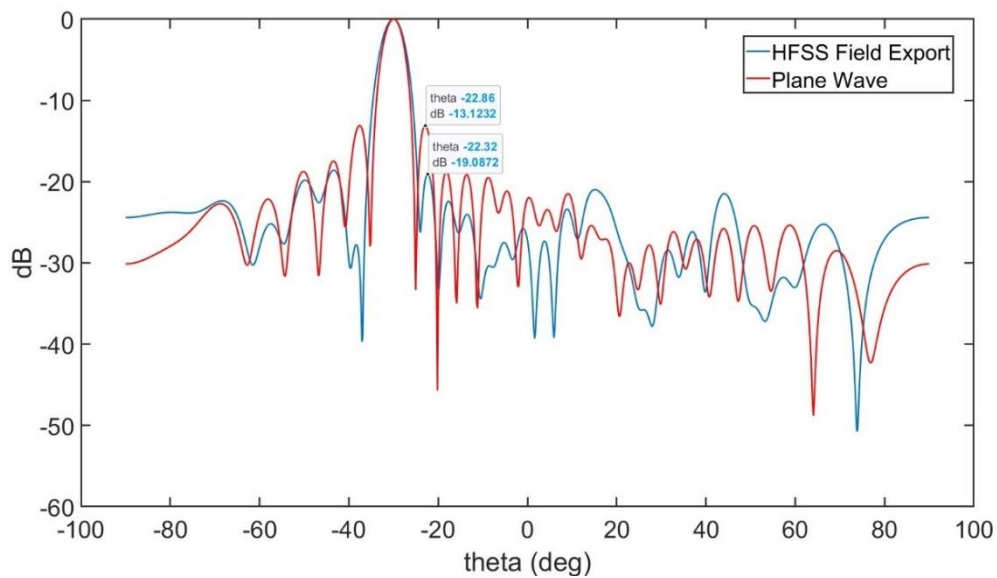
Figure 4.9: Comparing Analytical Array Factor of the 2 Different Types of Illuminations

The analytical array factor of the RIS are obtained using the MATLAB script. Two patterns are obtained; one assumes plane wave illumination on the RIS and the other uses the E-field's amplitude and phase information that was exported from HFSS. The

59

difference between the two patterns can be seen on figure 4.9. Plane wave illumination increases the directivity of the main beam, produces higher sidelobes, and have sharper nulls compared to the illumination from HFSS. This is caused almost entirely by the non-uniform amplitude of the E-field in the setup after passing through the lens. The phase of the E-field in HFSS is close to a plane wave. The formula to calculate the array factor (AF) is shown below.

$$AF_{RIS}(\theta, \phi) = \sum_{a=1}^{M} \sum_{b=1}^{N} \alpha_{ab} e^{-j\phi_{ab}^{total}} e^{-jk_o(x_a u + y_b v)} \tag{8}$$

Array size is MxN which for this RIS is 25x32. The u and v refer to the uv-plane which is $u = sin\theta cos\phi$ and $v = sin\theta sin\phi$. The x and y are the element position from the center of the RIS. α_{ab} is the amplitude factor which is just 1 for the uniform plane wave illumination or the amplitude tapering of the E-field exported from HFSS (maximum normalized to 1). The phase $\phi_{ab}^{total} = \phi_{ab}^{q} + \phi_{ab}^{illum} + \phi_{ab}^{rand}$ where ϕ_{ab}^{q} comes from the 1-bit quantization scheme using the PIN diode (either $0°$ or $180°$), ϕ_{ab}^{illum} is the phase of the illumination on the RIS which would be $0°$ everywhere for the uniform plane wave or whatever is exported out of HFSS, and ϕ_{ab}^{rand} are just additional random phases to remove the quantization lobe. The quantization lobe is another unwanted main beam that is symmetric in the opposite direction to the main beam. It is caused by only having a 1-bit quantization scheme.
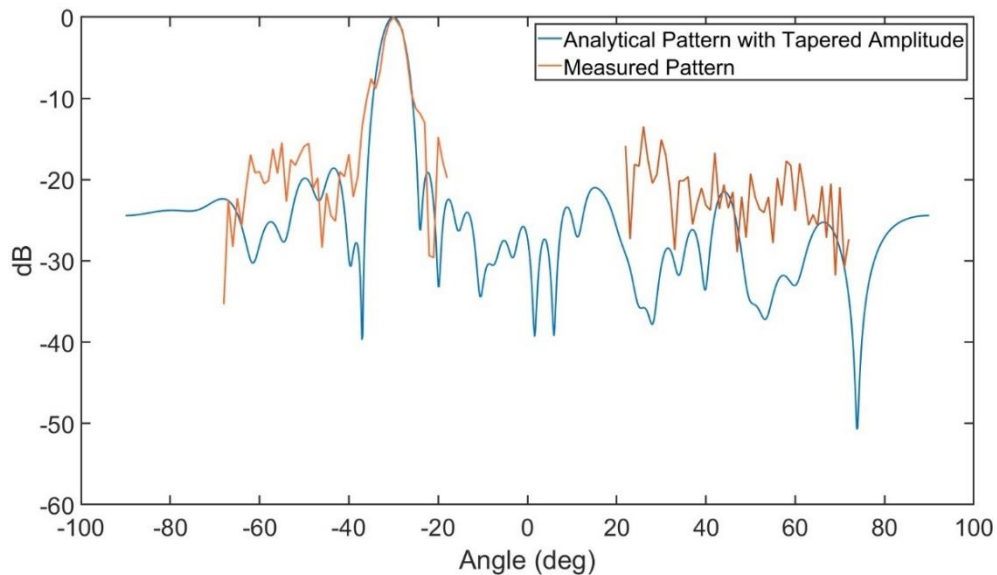
Figure 4.10: Comparison of Measured Pattern in Lab and Analytical Pattern with Tapered Amplitude Illumination Imported from HFSS

The normalized measured RCS pattern at 28.5 GHz is compared to the analytical pattern with tapered amplitude. The measured angle in lab was inverted in previous plots compared to the analytical plots but they have been made consistent in figure 4.10. In general, a uniform linear array has a SLL of -13 dB which can also be seen in figure 4.9. The SLL of the measured RCS pattern is lower at about -15 dB or -17 dB for the 2 sidelobes adjacent to the main beam which is expected. The noise floor of the spectrum analyzer is about -55 dBm and the maximum received power with the RIS is -24 dBm which gives about 30 dB of dynamic range to observe the sidelobes. Details in the sidelobes would have been lost in measurement even if everything else about the measurement setup was perfect due to limited dynamic range. There is also the matter of multipath interference arriving at the Rx antenna since the measurement was not performed in an anechoic chamber and there are miscellaneous objects present in lab. Other sources of interference at the Rx antenna include diffracted signals at the edge of

61

the lens (which travels in all directions) and reflected signals off the lens. This explains why the measured pattern has many jagged spikes where the sidelobes are supposed to be. Also, some details of the sidelobes will be missed because the goniometer only allows 1° increments which is coarse. However, the measurement setup can at least detect the main beam clearly and roughly detect the adjacent sidelobes.

CHAPTER 5

CONCLUSION

The measurement results show that the first prototype of the RIS has some issues with its performance. Its sidelobe at boresight is comparable in gain to the main lobe and the main lobe itself has a lower-than-expected gain when compared to the PEC reference. The second prototype of the RIS eliminates these issues with an increased gain of 2.54 dB for the main lobe when compared to the first prototype while also decreasing the side lobe at boresight to 22 dB below the main lobe.

Several flaws have been identified in the measurement setup through simulations and observations in the lab. Although the phase of the impinging beam on the RIS is constant enough to be considered in the far-field, the amplitude tapers off significantly at the edges of the RIS. This means that the beam is too focused by the lens and the RCS measurement will not accurately reflect the performance at far-field. Multipath interference arrives at the Rx antenna caused by reflection at the lens, diffraction at the edge of the lens and general clutter in the measurement environment. This increases the measurement error and prevents the sidelobes from being clearly identified. However, the SLL was lower than expected because of the tapered amplitude illumination. If there was uniform illumination on the RIS instead, the sidelobes should be high enough to be clearly detected even with this much interference in the environment.

There is future work to be done regarding the characterization of the RIS. The RIS measured here is a passive fixed-beam RIS made for the purpose of testing. The beamforming capabilities of an active RIS with PIN diodes still needs to be characterized

when it is fabricated. A microcontroller tunes the active RIS and its functions also need to be tested. The main issue with the current measurement setup is the non-uniform amplitude illumination which needs to be fixed to obtain accurate far-field RCS results. It is currently not possible to fix this issue with the resources in lab. A larger lens is desirable to increase the size of the quiet zone (at the cost of angular range of measurement) and a less focused lens to increase the waist of the beam to be around the same size as the RIS. Using a lower gain / wider beamwidth Tx antenna would also be preferrable if the size of the lens is increased. The illumination across the lens needs to be uniform to also have uniform amplitude across the quiet zone. If these two changes were applied, an anechoic chamber would need to be used because there is overspilling of signal at the lens and at the RIS.

REFERENCES

[1] C. Pan, H. Ren, K. Wang, J. F. Kolb, M. Elkashlan, M. Chen, M. Di Renzo, Y. Hao, J. Wang, A. L. Swindlehurst, X. You, and L. Hanzo, "Reconfigurable intelligent surfaces for 6G systems: Principles, applications, and Research Directions," IEEE Communications Magazine, vol. 59, no. 6, pp. 14–20, Jun. 2021.

[2] Q. Wu and R. Zhang, "Towards smart and reconfigurable environment: Intelligent Reflecting Surface Aided Wireless Network," IEEE Communications Magazine, vol. 58, no. 1, pp. 106–112, Jan. 2020.

[3] H. Kamoda, T. Iwasaki, J. Tsumochi, and T. Kuki, "60-GHz electrically reconfigurable reflectarray using P-i-N diode," 2009 IEEE MTT-S International Microwave Symposium Digest, 2009.

[4] B. G. Kashyap, P. C. Theofanopoulos, Y. Cui, and G. C. Trichopoulos, "Mitigating quantization lobes in mmwave low-bit reconfigurable reflective surfaces," IEEE Open Journal of Antennas and Propagation, vol. 1, pp. 604–614, 2020.

[5] J. Hu, H. Zhang, B. Di, L. Li, K. Bian, L. Song, Y. Li, Z. Han, and H. V. Poor, "Reconfigurable intelligent surface based RF sensing: Design, optimization, and implementation," IEEE Journal on Selected Areas in Communications, vol. 38, no. 11, pp. 2700–2716, Nov. 2020.

[6] L. Dai, B. Wang, M. Wang, X. Yang, J. Tan, S. Bi, S. Xu, F. Yang, Z. Chen, M. D. Renzo, C.-B. Chae, and L. Hanzo, "Reconfigurable intelligent surface-based wireless communications: Antenna Design, prototyping, and experimental results," IEEE Access, vol. 8, pp. 45913–45923, Mar. 2020.

[7] W. Tang, J. Y. Dai, M. Z. Chen, K.-K. Wong, X. Li, X. Zhao, S. Jin, Q. Cheng, and T. J. Cui, "MIMO transmission through reconfigurable intelligent surface: System design, analysis, and implementation," IEEE Journal on Selected Areas in Communications, vol. 38, no. 11, pp. 2683–2699, Nov. 2020.

[8] J.-B. Gros, V. Popov, M. A. Odit, V. Lenets, and G. Lerosey, "A reconfigurable intelligent surface at mmwave based on a binary phase tunable metasurface," IEEE Open Journal of the Communications Society, vol. 2, pp. 1055–1064, May 2021.

[9] X. Yuan, Y.-J. A. Zhang, Y. Shi, W. Yan, and H. Liu, "Reconfigurable-intelligent-surface empowered wireless communications: Challenges and opportunities," IEEE Wireless Communications, vol. 28, no. 2, pp. 136–143, Apr. 2021.

[10] V. Borkar, A. Ghosh, R. Singh, and N. Chourasia, "Radar cross-section measurement techniques," Defence Science Journal, vol. 60, no. 2, pp. 204–212, Feb. 2010.

[11] B. Ratni, A. de Lustrac, G.-P. Piau, and S. N. Burokur, "Reconfigurable meta-mirror for wavefronts control: Applications to microwave antennas," Optics Express, vol. 26, no. 3, pp. 2613–2624, Feb. 2018.

[12] M. F. Sundermeier and D. Fischer, "Compact radar cross-section measurement setup and performance evaluation," Advances in Radio Science, vol. 19, pp. 147–152, Dec. 2021.

[13] Hillbun, M., Martin, M. and Seabury, D., 2012. Single Antenna Measurement Using Gated Time Domain and The Mirror Method. [online] In Compliance Mag. Available at: <https://incompliancemag.com/article/single-antenna-measurement-using-gated-time-domain-and-the-mirror-method/>.

[14] C. A. Balanis, Antenna theory: Analysis and design. Hoboken, NJ: Wiley, 2016.

[15] W. R. Kruesi and I. N. Howell, IEEE Standard Test Procedures for antennas. New York, NY: IEEE, 1979.